

# Unsteady flow separation on slip boundaries

François Lekien<sup>1,a)</sup> and George Haller<sup>2</sup>

<sup>1</sup>École Polytechnique, Université Libre de Bruxelles, CP 165/11, B-1050 Brussels, Belgium

<sup>2</sup>Department of Mechanical Engineering, Massachusetts Institute of Technology, Cambridge Massachusetts 02139, USA

(Received 1 June 2007; accepted 17 December 2007; published online 3 September 2008)

We derive analytic criteria for the location and angle of unsteady particle separation and reattachment in two-dimensional flows with free-slip boundary conditions. Our wall-based criteria show that, in general, fluid breakaway from the boundary takes place at locations different from either instantaneous or averaged stagnation points. Indeed, for time-varying flows, separation does not occur along a free streamline or along an average free streamline. We apply the formula to transport in randomized Rayleigh–Bénard convection cells, as well as to boundary current separation and reattachment in high-frequency radar data collected in Monterey Bay, California.

© 2008 American Institute of Physics. [DOI: [10.1063/1.2923193](https://doi.org/10.1063/1.2923193)]

## I. INTRODUCTION

Flow separation is the breakaway of fluid from a solid boundary. From aerodynamic stall through oceanic boundary current separation to microfluidic mixing, a variety of fluid flows are dominated by separating flow structures. In a seminal paper on two-dimensional steady flows with no-slip boundaries, Prandtl showed that separation takes place at points of zero wall-shear and negative wall-shear gradients.<sup>1</sup> A major open question has been how Prandtl's criterion could be generalized to unsteady flows.

Early work on two-dimensional unsteady flows revealed that *vanishing wall shear and accompanying flow reversal near the wall does not, in general, denote separation in any meaningful sense in unsteady flows* with no-slip boundaries.<sup>2,3</sup> Indeed, numerical simulations and experimental flow visualization using smoke, dye, or tracers indicate fluid breakaway at locations unrelated to instantaneous points of zero wall shear.<sup>3,4</sup> For separation taking place exactly on the boundary, a necessary and sufficient criterion for particle separation exists.<sup>5</sup> Nevertheless, this result is limited to no-slip boundaries and is unable to represent more complex separation processes where fluid detaches at a finite distance from the boundary (see, for example, the experiments of Koromilas and Telionis<sup>6</sup>).

To capture global boundary layer separation, it is convenient to observe the flow at a lower resolution. This procedure is commonly used in large-scale geophysical simulations, such as ocean or mantle modeling. In such systems, the grid resolution of the numerical solver cannot usually be made sufficiently small to resolve the boundary layer. In the discretized equations, the first row of grid points along the boundary represents the averaged motion in the boundary layer instead of the boundary itself. At such a low resolution, enforcing the usual no-slip boundary condition (all the components of the velocity vanish) is therefore not appropriate. Instead, it is replaced by the weaker *free-slip boundary condition* (the normal component of the velocity vanishes but

particles can move freely along the boundary). It is worth noting that switching to a low resolution free-slip model is not only a necessary evil resulting from the limited amount of memory available on today's computers, but is also a means to study global separation of the boundary layer. Indeed, when many complex processes occur inside the boundary layer,<sup>6</sup> the free-slip model maps the net boundary layer behavior to the free-slip boundary.

Two objectives are therefore pursued in this manuscript on separation and reattachment along free-slip boundaries. First, we provide a free-slip theory that can be applied directly to ocean and plasma large-scale problems where only data with free-slip boundary conditions are available. Second, the free-slip theory also gives the means to “look at the fluid problem from a distance” and to investigate separation of the entire boundary layer.

Unsteady separation in flows with slip boundaries has not yet been scrutinized as much as separation on no-slip boundaries. Motivated by two-dimensional steady slip flows, most studies associate unsteady slip separation with free streamlines detaching from the wall or, equivalently, instantaneous hyperbolic stagnation points on the wall. Related work on geophysical flows shows, however, a vast discrepancy between wall-based stagnation points and locations of tracer breakaway in unsteady flows.<sup>7,8</sup>

Few theoretical studies have been concerned with the details of unsteady slip separation. Ghil *et al.* gave conditions under which bifurcation creates an instantaneous stagnation point on the boundary.<sup>9</sup> In unsteady flows, however, stagnation points do not mark the locations of Lagrangian separation, the actual fluid breakaway.

Iterative procedures for locating Lagrangian separation and reattachment points near a stagnation point on a free-slip boundary have been proposed.<sup>10,11</sup> Separation may not, however, take place near a stagnation point if this point bifurcates or moves fast enough.<sup>12</sup> Conversely, flow separation can also occur in the absence of stagnation points on the boundary. Figure 1 shows pathlines for an unsteady flow in a circular domain. This flow has closed streamline contours at each

<sup>a)</sup>Electronic mail: lekien@ulb.ac.be.

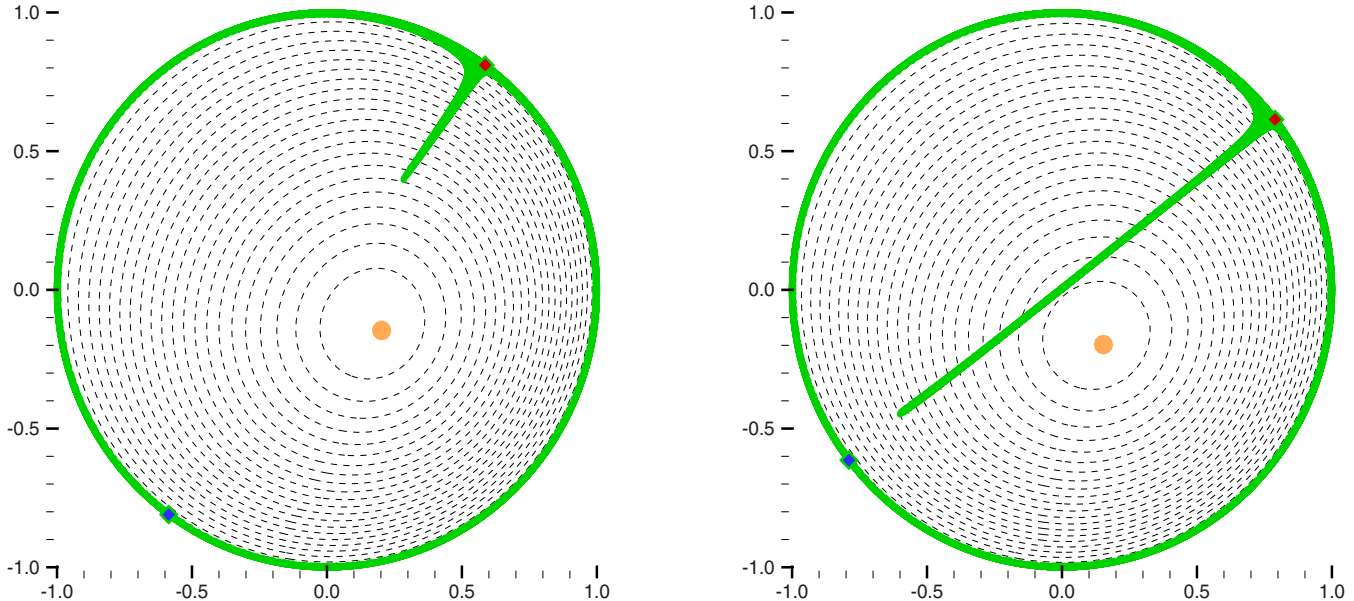


FIG. 1. (Color online) Separation in the absence of hyperbolic stagnation points and without any free streamline detaching from the boundary. The streamfunction is given by  $\psi(x,y,t)=(x^2+y^2-1)(x \cos \omega t+y \sin \omega t+\omega/2)$ . For  $\omega>2$ , the streamlines are closed curves (dashed lines) and there is only one elliptic stagnation point oscillating near the origin. Numerical pathlines and analytical solutions reveal flow separation from the boundary, which has neither stagnation points nor detaching streamlines. The figure corresponds to  $\omega=4$  (enhanced online).

time instance and does not have any stagnation points on the boundary. There is not any free streamline detaching from the boundary. Nevertheless, a thin material spike starting from the boundary reveals the presence of flow separation.<sup>13,14</sup> Examples such as this one underline how separation is inherently a Lagrangian concept: The process is defined by the motion of *particles detaching from the boundary*. In slowly varying flows, separating lines of particles and free streamlines are sufficiently close to approximate the former with the latter. Examples like the one depicted in Fig. 1 show that for quickly varying flows, actual particle separation may be unrelated to streamlines detaching from the boundary. The same conclusion holds for stagnation points. Hence, we seek a separation criterion that does not rely on instantaneous stagnation points or on streamline geometry. Instead, we concentrate on the motion of particles: Separation is the concentration of particles on and near the boundary, followed by ejection of a material spike inside the flow.

Lekien *et al.*<sup>15</sup> computed slip separation and reattachment points from a finite-time Lyapunov exponent analysis. This procedure yields correct breakaway locations, but it relies on the global tracking of fluid particles away from the boundary. In some applications, on-wall detection of separation is preferred, if not required. Moreover, Lyapunov exponent studies do not yield explicit separation criteria in terms of familiar boundary quantities.

Despite the lack of a complete theory, unsteady separation on slip boundaries occurs in many applications. Examples include boundary current separation in oceanic flows,<sup>16,17</sup> recirculation in coastal areas,<sup>18</sup> wake formation behind moving bubbles,<sup>19,20</sup> vortex shedding in the wake of a fish fin<sup>21</sup> recirculation in microfluidic devices,<sup>22,23</sup> and lift generation on free-flying insects.<sup>24</sup> In most of these ex-

amples, the fluid velocity on the boundary is not prescribed (free slip). In many other examples, the global separation of the boundary layer of a true no-slip flow can be studied efficiently by switching to a free-slip model.

In this paper, we present necessary and sufficient criteria for slip separation in two-dimensional unsteady flows. Using the theory of normally hyperbolic invariant manifolds from dynamical system theory, we derive explicit time-dependent formulas for the separation location and angle. At separation, attracting material lines (unstable manifolds) emerge from the boundary, collecting fluid particles from the vicinity of the boundary, then subsequently ejecting them into the main stream. We obtain similar results for flow reattachment by locating repelling material lines (stable manifolds) that collect and guide fluid from the main stream to stretch it along the boundary.

To illustrate our results, we first consider the two-dimensional Rayleigh–Bénard convection model of Solomon and Gollub<sup>25</sup> with a periodic motion of the roll pattern. In this case, separation is well understood since the separation points are the invariants of the Poincaré map—a stroboscopic view of particle paths in the system.<sup>26</sup> We show that, for the periodic case, our separation theory is equivalent to classical results. We then prescribe random motion for the roll pattern in the Solomon–Gollub model and add Gaussian noise to test the robustness of the separation criteria to perturbations. Our aim is to locate separation from, and reattachment to, horizontal convection cell boundaries. We find that separation and reattachment points differ markedly from the randomly appearing instantaneous stagnation points and from the stagnation points of the mean flow.

As a first application, we consider separation profiles computed by Coulibert and Wiggins<sup>8</sup> for the quasigeo-

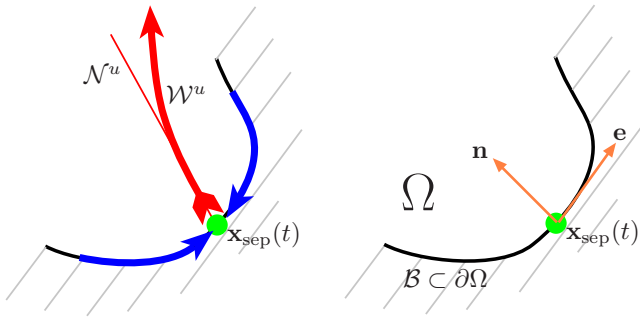


FIG. 2. (Color online) Separation is the breakaway of fluid near a wall. Particles in  $\mathcal{B}$ , a portion of the boundary that acts as a stable manifold, are attracted toward the separation trajectory  $x_{sep}(t)$ . Fluid is ejected along an unstable manifold  $\mathcal{W}^u$  inside the fluid domain  $\Omega$ . A necessary and sufficient criteria for separation is derived by transforming the velocity field into a moving coordinate frame oriented with the unit tangent vector  $e$  and the unit normal vector  $n$ . The existence of a normally hyperbolic subspace  $N^u$  generates the desired separation framework.

strophic ocean model of Rowley<sup>27</sup> and we show that our formulas predict the previously observed separation angle. Finally, we consider velocity data obtained from the coastal ocean dynamics applications radar (CODAR) installation in Monterey Bay, CA. The separation and reattachment points that we identify agree with previous studies.<sup>7</sup> The originality of the present work is that we use only coastal velocities in predicting separation and reattachment angles and hence obtain our results at a significantly reduced computational cost.

## II. SETUP

Consider a two-dimensional fluid velocity field

$$\mathbf{v}(\mathbf{x}, t) = \begin{pmatrix} u(x, y, t) \\ v(x, y, t) \end{pmatrix},$$

with  $\mathbf{x} = (x, y)$  defined on a smooth planar domain  $\Omega$  that is allowed to vary in time (see Fig. 2). We assume that the first spatial derivatives of  $\mathbf{v}(\mathbf{x}, t)$  are uniformly bounded in time.

We also assume that, on a (possibly time-dependent) smooth compact subset  $\mathcal{B}$  of the flow boundary  $\partial\Omega$ , the velocity field satisfies the free-slip boundary condition

$$\langle \mathbf{v}(\mathbf{x}, t), \mathbf{n}(\mathbf{x}, t) \rangle = 0, \quad \mathbf{x} \in \mathcal{B}, \quad (1)$$

where  $\mathbf{n}(\mathbf{x}, t)$  denotes the inward unit normal to  $\mathcal{B}$  and  $\langle \cdot, \cdot \rangle$  is the inner product. The condition above states that the velocity field is tangent to  $\mathcal{B}$ . Trajectories starting on the compact boundary segment  $\mathcal{B}$  are confined to  $\mathcal{B}$  and hence remain bounded at all times. Let  $\mathbf{e}(\mathbf{x}, t)$  denote the unit tangent vector to  $\mathcal{B}$  at point  $\mathbf{x}$  and at time  $t$  for which

$$\det[\mathbf{e}(\mathbf{x}, t) \quad \mathbf{n}(\mathbf{x}, t)] = 1.$$

Fluid trajectories  $\mathbf{x}(t)$  generated by the velocity field satisfy the differential equation

$$\dot{\mathbf{x}} = \mathbf{v}(\mathbf{x}, t). \quad (2)$$

For simplicity, we assume planar flow geometry, but the results obtained extend to flows on any smooth, orientable, two-dimensional surfaces, such as a sphere or an isopycnal surface in the ocean.

## III. FREE-SLIP SEPARATION AND REATTACHMENT

In this section, we define unsteady flow separation from, and reattachment to, the free-slip boundary segment  $\mathcal{B}$ . We then derive necessary and sufficient criteria under which separation or reattachment occurs.

### A. Definitions

We say that *flow separation* takes place on  $\mathcal{B}$  along a boundary trajectory  $\mathbf{x}(t)$  if

[S1]  $\mathbf{x}(t)$  attracts other trajectories within  $\mathcal{B}$ ;

[S2]  $\mathbf{x}(t)$  has a unique unstable manifold  $\mathcal{W}^u[\mathbf{x}(t)]$  that is uniformly bounded away from a portion of boundary containing  $\mathbf{x}(t)$  in backward time;

[S3] the above two properties are robust: Small enough smooth perturbations to the velocity field result in a nearby  $\mathbf{x}(t)$  satisfying S1 and S2.

Conditions S1 and S2 describe experimentally observed features of flow separation: Particles converge to the separation location along the wall and then are ejected from the wall (see Fig. 2 as well as the illustrations of Koromikas and Telionis<sup>6</sup> for a geometric description of this setting). Physically, the unstable manifold  $\mathcal{W}^u[\mathbf{x}(t)]$  is a material line that shrinks to  $\mathbf{x}(t)$  in backward time. Condition S3 guarantees the observability of the separation taking place along  $\mathcal{W}^u[\mathbf{x}(t)]$ . This definition of separation is compatible with previous work on slip separation<sup>28</sup> as well as no-slip separation.<sup>5</sup>

We also define *reattachment* as separation in backward time. Specifically, reattachment takes place along a boundary trajectory  $\mathbf{x}(t)$  if

[R1]  $\mathbf{x}(t)$  repels other trajectories within  $\mathcal{B}$ ;

[R2]  $\mathbf{x}(t)$  has a unique stable manifold  $\mathcal{W}^s[\mathbf{x}(t)]$  that is uniformly bounded away from a portion of boundary containing  $\mathbf{x}(t)$  in forward time;

[R3] the above two properties are robust.

In this case, the stable manifold  $\mathcal{W}^s[\mathbf{x}(t)]$  is a material line that shrinks to  $\mathbf{x}(t)$  in forward time.

### B. Separation and reattachment criteria

As we prove in Appendix A, flow separation takes place along a boundary trajectory  $\mathbf{x}(t)$  up to the present time  $t$  whenever

$$\lambda_e(t) = \limsup_{T \rightarrow +\infty} \frac{1}{T} \int_{t-T}^t \langle \mathbf{e}, (\nabla \mathbf{v}) \mathbf{e} \rangle_{[\mathbf{x}(s), s]} ds < 0, \quad (3)$$

$$\lambda_n(t) = \liminf_{T \rightarrow +\infty} \frac{1}{T} \int_{t-T}^t \langle \mathbf{n}, (\nabla \mathbf{v}) \mathbf{n} \rangle_{[\mathbf{x}(s), s]} ds > 0,$$

with  $\langle \cdot, \cdot \rangle$  denoting the inner product. For incompressible flows,  $\langle \mathbf{n}, (\nabla \mathbf{v}) \mathbf{n} \rangle = -\langle \mathbf{e}, (\nabla \mathbf{v}) \mathbf{e} \rangle$ ; thus, Eq. (3) simplifies into  $\lambda_n(t) > 0$  or, equivalently,  $\lambda_e(t) < 0$ . In fact, provided that the density remains uniformly bounded from both zero and infinity, Appendix B shows that we can always check only one of the two conditions  $\lambda_e < 0$  or  $\lambda_n > 0$ .

Physically, the conditions in Eq. (3) require the averaged tangential rate of strain  $\lambda_e$  and the averaged normal rate of

strain  $\lambda_n$  along a boundary trajectory  $\mathbf{x}(t)$  to be asymptotically negative and positive, respectively. A strict asymptotic average for these strain rates may not exist, hence the use of “lim sup” and “lim inf” instead of a simple limit.

We also show in Appendix A that under the conditions (3), the separation angle  $\theta(t)$  measured from the boundary satisfies

$$\cot \theta = \lim_{T \rightarrow +\infty} \int_{t-T}^t e^{\int_s^t [\langle \mathbf{e}, (\nabla \mathbf{v}) \mathbf{e} \rangle - \langle \mathbf{n}, (\nabla \mathbf{v}) \mathbf{n} \rangle]_{[\mathbf{x}(r), r]} dr} [\langle \mathbf{e}, (\nabla \mathbf{v}) \mathbf{n} \rangle + \langle \mathbf{n}, (\nabla \mathbf{v}) \mathbf{e} \rangle]_{[\mathbf{x}(s), s]} ds. \quad (4)$$

Similarly, reattachment takes place along a boundary trajectory  $\mathbf{x}(t)$  from the present time  $t$  whenever

$$\begin{aligned} \lambda_e(t) &= \liminf_{T \rightarrow +\infty} \frac{1}{T} \int_t^{t+T} \langle \mathbf{e}, (\nabla \mathbf{v}) \mathbf{e} \rangle_{[\mathbf{x}(s), s]} ds > 0, \\ \lambda_n(t) &= \limsup_{T \rightarrow +\infty} \frac{1}{T} \int_t^{t+T} \langle \mathbf{n}, (\nabla \mathbf{v}) \mathbf{n} \rangle_{[\mathbf{x}(s), s]} ds < 0. \end{aligned} \quad (5)$$

For incompressible flows, Eq. (5) simplifies to the single condition  $\lambda_n < 0$ . Appendix B shows that for fluids with densities uniformly bounded away from zero and infinity, one condition also implies the other. It is therefore enough to check only one of  $\lambda_e > 0$  or  $\lambda_n < 0$ . Furthermore, at any time  $t$ , the reattachment angle  $\theta(t)$  measured from the boundary satisfies

$$\cot \theta = - \lim_{T \rightarrow +\infty} \int_t^{t+T} e^{\int_s^t [\langle \mathbf{n}, (\nabla \mathbf{v}) \mathbf{n} \rangle - \langle \mathbf{e}, (\nabla \mathbf{v}) \mathbf{e} \rangle]_{[\mathbf{x}(r), r]} dr} \times [\langle \mathbf{e}, (\nabla \mathbf{v}) \mathbf{n} \rangle + \langle \mathbf{n}, (\nabla \mathbf{v}) \mathbf{e} \rangle]_{[\mathbf{x}(s), s]} ds. \quad (6)$$

### C. Numerical implementation of the criteria

Implementing the separation and reattachment criteria in Eqs. (3) and (5) requires the computation of  $\lambda_n$  and  $\lambda_e$  for an array of trajectories on the boundary segment of interest. Trajectories satisfying the two conditions in either Eq. (3) or (5) are locally unique by the theory of normally hyperbolic invariant manifolds (cf. Appendix A). For such trajectories, formulas (4) and (6) give the correct separation or reattachment angles.

In practice, however, velocity data are available only for finite time intervals; thus, the asymptotic expressions in criteria (3) and (5), as well as in angle formulas (4) and (6), cannot be computed exactly. Instead, we invoke earlier results on finite-time hyperbolic material lines<sup>12,14,29</sup> to conclude that finite-time versions of Eqs. (3) and (5) mark moving separation or reattachment points over a finite-time interval  $T$ .

Such boundary trajectories are no longer unique, but all tend exponentially fast to a well-defined unique trajectory as the length of the available velocity data increases.<sup>12</sup> Consequently, separation and reattachment points identified from finite-time versions of Eqs. (3) and (5) will be unique for practical purposes, at least when computed from long enough velocity data.

In view of the above, at any time  $t$  and for large enough  $T$ , we identify a separation point candidate  $\mathbf{x}(t)$  as a positive local maximum of  $\lambda_n(t)$ . The boundary trajectory  $\mathbf{x}(t)$  is an actual moving separation point if it also satisfies  $\lambda_e(t) < 0$ . For incompressible flows,  $\lambda_e(t) < 0$  holds whenever  $\lambda_n(t) > 0$ ; thus, only one of the two conditions in Eq. (3) has to be verified. Appendix B shows that the equivalence holds also for most compressible fluids where the density is uniformly bounded away from 0 and  $+\infty$ .

According to the criterion in Eq. (5), locating reattachment at a given time requires the knowledge of future velocity information. Hence, given a finite-time data set up to time  $t_f$  and a constant integration time  $T$ , we can obtain only approximate reattachment locations at times  $t < t_f - T$  as positive local maxima of  $\int_t^{t+T} \langle \mathbf{e}, (\nabla \mathbf{v}) \mathbf{e} \rangle_{[\mathbf{x}(s), s]} ds$  and negative local minima of  $\int_t^{t+T} \langle \mathbf{n}, (\nabla \mathbf{v}) \mathbf{n} \rangle_{[\mathbf{x}(s), s]} ds$ .

The minima and maxima that we compute approximate separation trajectories with an arbitrary precision, provided that the integration time  $T$  is long enough. For small  $T$ , the minima and maxima are not true trajectories and might even bifurcate at some times. Such bifurcating approximate separation points are often desirable in systems that oscillate between different dynamical regimes.<sup>13,30</sup>

Note that our separation criteria require only the knowledge of the velocity and velocity derivatives on the boundary. This is a useful feature for experimental implementation and flow control applications. To use the separation criterion, it is not necessary to install sensors in the flow to study and control separation; it is sufficient to place captors on the wing, airfoil, or other surface of interest.

### IV. EXAMPLE 1: PERIODICALLY OSCILLATING RAYLEIGH–BÉNARD CONVECTION

We illustrate the use of our separation and reattachment criteria on a two-dimensional model of time-dependent Rayleigh–Bénard convection developed by Solomon and Golub.<sup>25,31,32</sup> This model involves an infinite array of convection cells and hence does not have any real solid boundaries. Nevertheless, each convection cell is bounded from above and below by horizontal streamlines that behave as free-slip walls. Our objective is to find the locations of separation from, and reattachment to, these horizontal cell boundaries.

The Rayleigh–Bénard convection model of Solomon and Golub<sup>25</sup> is given by the streamfunction

$$\psi = \frac{A}{k} \sin\{k[x - g(t)]\} \sin 2y, \quad (7)$$

where  $A$  is the maximum vertical velocity in the flow,  $k$  is the wave number, and  $g(t)$  represents the lateral motion of the roll pattern. The domain of the fluid is defined by  $x \in \mathbb{R}$  and  $0 \leq y \leq \pi/2$ . The lines  $y=0$  and  $y=\pi/2$  are the free slip boundaries of the system.

In the velocity field generated by  $\psi$ , the fluid rotates in opposite directions in adjacent cells. In the absence of roll motion ( $g(t)=K$ ), the boundaries between cells are vertical lines satisfying  $x=K+\pi/k$ . In this case, cell-to-cell transport is possible only through diffusion. For nonzero roll velocity,

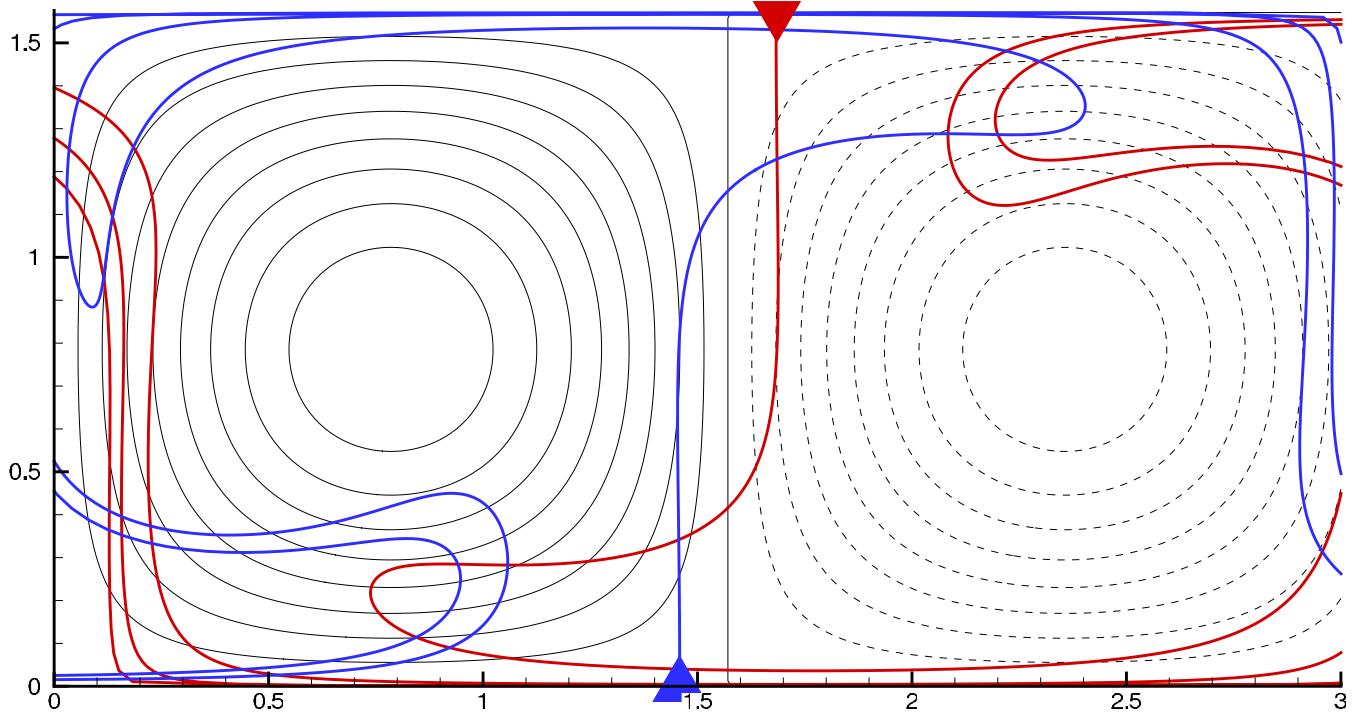


FIG. 3. (Color online) Separation in periodically oscillating convection cells. The invariants of the Poincaré map of the system correspond to periodic hyperbolic trajectories on the top and bottom boundaries (triangles). The flow separates along the unstable manifold of the hyperbolic trajectory oscillating along the top boundary. Particles reattach to the lower boundary along the unstable manifold of the other hyperbolic trajectory.

the vertical lines between cells move at a speed  $\dot{g}(t)$  and are no longer barriers to transport (see Fig. 3). In this case, cell-to-cell transport is dominated by chaotic advection.<sup>33</sup>

Camassa and Wiggins<sup>28</sup> studied Lagrangian transport between cells for periodic oscillations  $g(t)=B \sin(\omega t)$ . In this case, separation and reattachment on the horizontal walls take place along stable and unstable manifolds of periodic fluid trajectories that are confined to those walls. Such periodic trajectories are fixed points of the associated Poincaré map. Their stable and unstable manifolds intersect and form heteroclinic tangles that are responsible for chaotic cell-to-cell transport (see Fig. 3). Following the transport theory of Rom-Kedar near a heteroclinic tangle,<sup>26</sup> cell-to-cell fluxes and re-entry rates can be efficiently computed based on the geometry and the area of the lobes comprised between the invariant manifolds.

For a periodic motion of the roll pattern, this system is therefore well understood using classical tools such as Poincaré sections. The separation and reattachment points are periodic trajectories that can be computed by seeking invariants in the Poincaré sections of the boundaries. The periodic oscillation of such a Poincaré invariant along the top boundary (see Fig. 3) is shown on the left panel of Fig. 4. To compare the criteria that we develop in this manuscript with the classical Poincaré analysis for periodic flows, we have superimposed the curve corresponding to the maximum of  $\lambda_n$  for this system (see left panel of Fig. 4). The two resulting curves are visually identical, which indicates that our criteria reduce to the classical Poincaré invariant for periodic flows. The right panel of Fig. 4 shows that the difference between

the two approaches remains below 0.1% of the amplitude of the motion of the separation point.

Note that the implementation of criteria (3) and (5) require the selection of a large (but finite) integration time  $T$ . The results shown in Fig. 4 are independent of the choice of  $T$ , which need not be an integer multiple of the period of the flow. Provided that  $T$  is large enough (i.e., larger than 2 or 3 times the period of the flow), criteria (3) and (5) reduce to the classical Poincaré invariant for periodic flows.

## V. EXAMPLE 2: RANDOMLY OSCILLATING RAYLEIGH-BÉNARD CONVECTION

Our objective is to locate separation and reattachment on the horizontal cell boundaries when the time dependence is aperiodic and, hence, Poincaré maps are undefined. To illustrate the generality of our separation criteria, we consider the same model of Rayleigh-Bénard convection [see Eq. (7)] where we use a smooth but aperiodic function  $g(t)$  in Eq. (7) to emulate the temporal complexity of turbulent convection.

Specifically,  $g(t)$  is a realization of a random process with zero mean (i.e.,  $E[g(t)]=0$ ), variance  $B$  (i.e.,  $E[g(t)^2]=B$  for all  $t$ ), and stationary Gaussian covariance in time,

$$E[g(t_1)g(t_2)] = Be^{-|t_1 - t_2|^2/\tau_0^2}, \quad (8)$$

where  $\tau_0$  is the decorrelation time, i.e., the typical time scale of the random oscillations of  $g(t)$ .

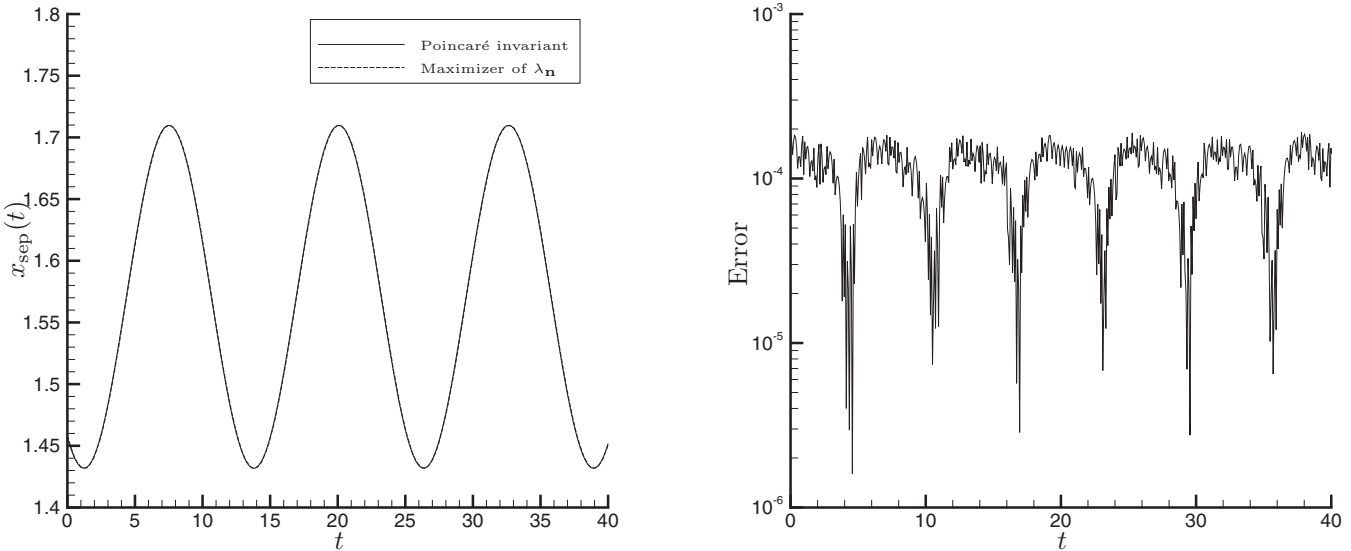


FIG. 4. Comparison between the hyperbolic Poincaré invariants (classical theory) and the point corresponding to the maximum  $\lambda_n$  for periodic Rayleigh–Bénard convection cells. Left panel: The Poincaré section of the system has invariants that correspond to hyperbolic (separating) periodic trajectories. The maximum of  $\lambda_n$  is visually identical to the separation point predicted by Poincaré. Right panel: The difference between Poincaré’s separating trajectory and the point where  $\lambda_n$  is maximum, remains below 0.1% of the amplitude of the oscillations regardless of the integration time  $T$ .

We generate the random function  $g(t)$  using the Wiener–Khintchine theorem.<sup>34</sup> Namely, we first generate a random Fourier spectrum  $G(\omega)$  with zero mean and unit impulse covariance  $E[G(\omega)G(\omega')] = \delta(\omega - \omega')$ . Such a spectrum can be computed at discrete points  $\omega_i$  using a random number generator because the spectrum is uncorrelated [i.e., the value of  $G(\omega_i)$  can be selected independently of  $G(\omega_j)$  with  $\omega_j \neq \omega_i$ ]. We then obtain  $g(t)$  by inverting the random spectrum  $G(\omega)$  with the desired Gaussian covariance,

$$g(t) = \frac{B}{2\pi} \operatorname{Re} \left[ \int_{-\infty}^{+\infty} G(\omega) e^{-2\pi\omega^2 \tau_0^2 + i\omega t} d\omega \right]. \quad (9)$$

As an example, Fig. 5 shows a realization of the lateral motion of the roll pattern (solid curve) for  $B=0.48$  and  $\tau_0=\pi$ . For numerical simulations, the right-hand side of Eq. (9) is replaced by a discrete spectrum with a large number of components. The algorithm used to compute the Gaussian noise is available online.<sup>35</sup> Note that  $g(t)$  is a (deterministic) realization of the random process and is not itself a random variable. The Gaussian noise is introduced only to produce a smooth but aperiodic function  $g(t)$  with a specified timescale. Once computed,  $g(t)$  is considered deterministic and not stochastic.

The velocity field generated by the streamfunction (7) is incompressible; hence, the separation and reattachment criteria simplify to the second equations in Eqs. (3) and (5). On both horizontal streamlines ( $y=0$  and  $y=\pi/2$ ), a direct computation gives

$$\langle \mathbf{n}, (\nabla \mathbf{v}) \mathbf{n} \rangle = v_y = -\frac{\partial^2 \psi}{\partial x \partial y} = -2A \cos\{k[x - g(t)]\} \cos 2y,$$

which we integrate in time along boundary trajectories to evaluate Eqs. (3) and (5). Note that only velocity and velocity gradient information on the boundary are needed to perform this analysis.

Figures 6–8 show the streamlines of the model with random  $g(t)$  at three different times  $t$ . For different integration

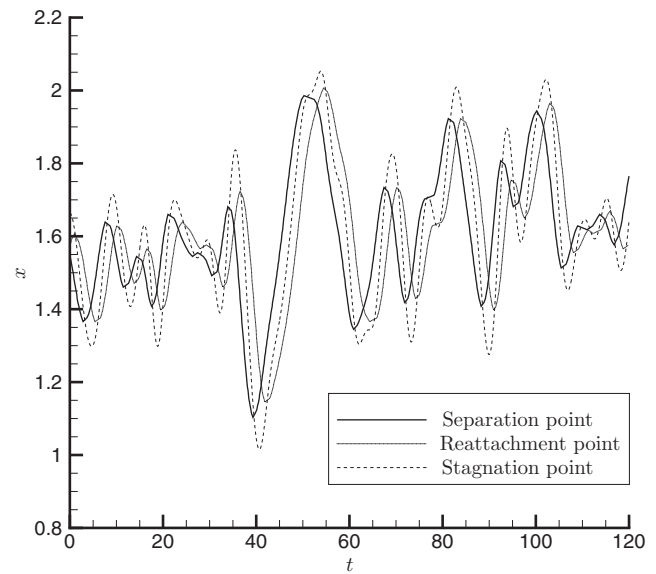


FIG. 5. Amplitude of the random forcing  $g(t)$  (which also corresponds to a stagnation point in this case) and corresponding separation and reattachment points. This chart gives only the  $x$  coordinate of the points. For the separation point, the  $y$  coordinate is  $y=\pi/2$ . For the reattachment point, the  $y$  coordinate is  $y=0$ . Note that  $g(t)$ , shifted by  $\pi/2$ , corresponds to the  $x$  coordinates of the stagnation points both on the top and on the bottom boundaries.

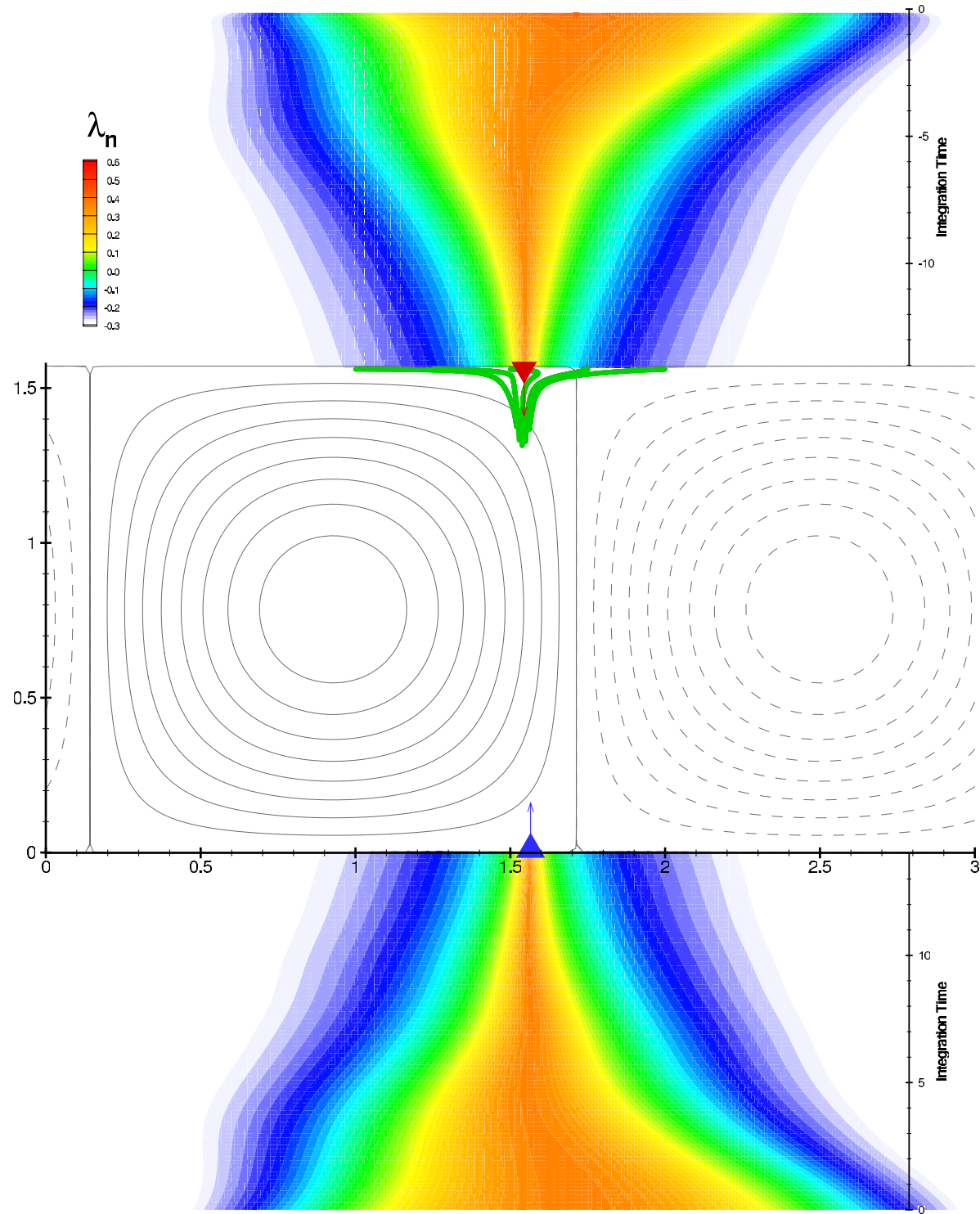


FIG. 6. (Color online) Transport in a chaotic Rayleigh–Bénard cell under random Gaussian forcing with amplitude  $B=0.48$  and decorrelation time  $\tau_0=\pi$ . Figures 6–8 show streamlines [Eq. (7) with  $A=0.18$  and  $k=2$ ], as well as separation and reattachment points at different times. Also shown are the  $\lambda_n$  fields in forward (below streamlines) and backward time (above streamlines). The color map is identical for the two  $\lambda_n$  plots and their maxima mark separation or reattachment. Particles (thick lines) released from five fixed locations near the top boundary confirm the predicted position and angle of separation. This panel corresponds to time  $t=5$ .

times  $T$ , Figs. 6–8 show also a color map of  $\lambda_n$ , which we view as a function of initial trajectory positions along the top and bottom cell boundaries ( $y=0$  and  $y=\pi/2$ ). As the integration time increases, only one point on each boundary continues to admit a positive  $\lambda_n$ . This point corresponds to a

separation point on the top cell boundary, and a reattachment point on the bottom cell boundary.

The angle between the boundary and the separation (or reattachment) profile at each of these points can be computed using formulas (4) and (6). Since we have

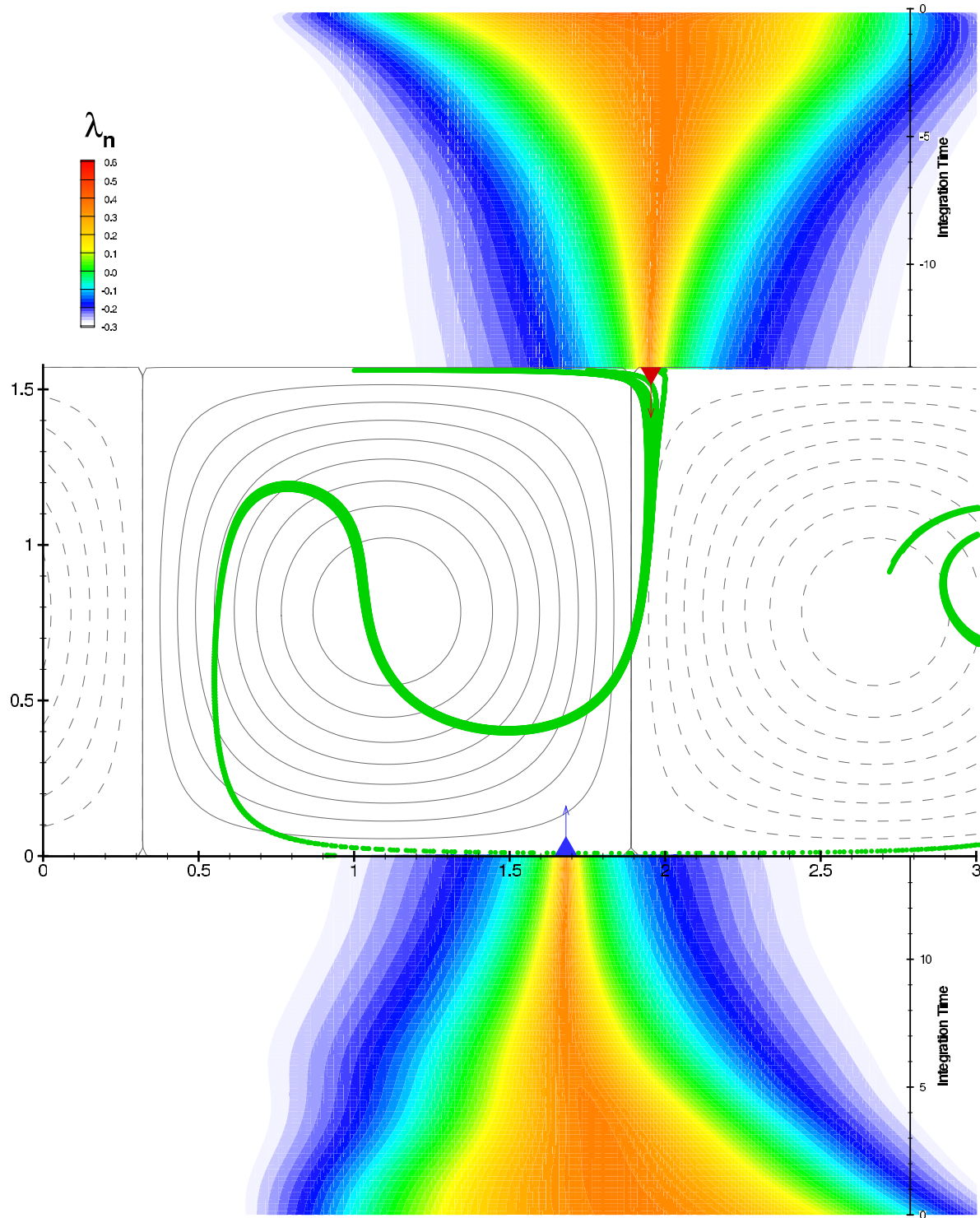


FIG. 7. (Color online) Transport in a chaotic Rayleigh–Bénard cell under random Gaussian forcing with amplitude  $B=0.48$  and decorrelation time  $\tau_0=\pi$ . Figures 6–8 show streamlines [Eq. (7) with  $A=0.18$  and  $k=2$ ], as well as separation and reattachment points at different times. Also shown are the  $\lambda_n$  fields in forward (below streamlines) and backward time (above streamlines). The color map is identical for the two  $\lambda_n$  plots and their maxima mark separation or reattachment. Particles (thick lines) released from five fixed locations near the top boundary confirm the predicted position and angle of separation. This panel corresponds to time  $t=30$ .

$$\begin{aligned} \langle \mathbf{e}, (\nabla \mathbf{v}) \mathbf{n} \rangle + \langle \mathbf{n}, (\nabla \mathbf{v}) \mathbf{e} \rangle &= u_y + v_x \\ &= \frac{A}{k} (k^2 - 4) \sin\{k[x - g(t)]\} \sin 2y, \end{aligned}$$

the integrands in Eqs. (4) and (6) vanish identically on the

top and bottom cell boundaries where  $y=0$  or  $y=\pi/2$ . We therefore conclude that  $\theta=\pi/2$ , i.e., the separation and reattachment profiles are always locally orthogonal to the cell boundaries.

To verify the above predictions, we show advected fluid

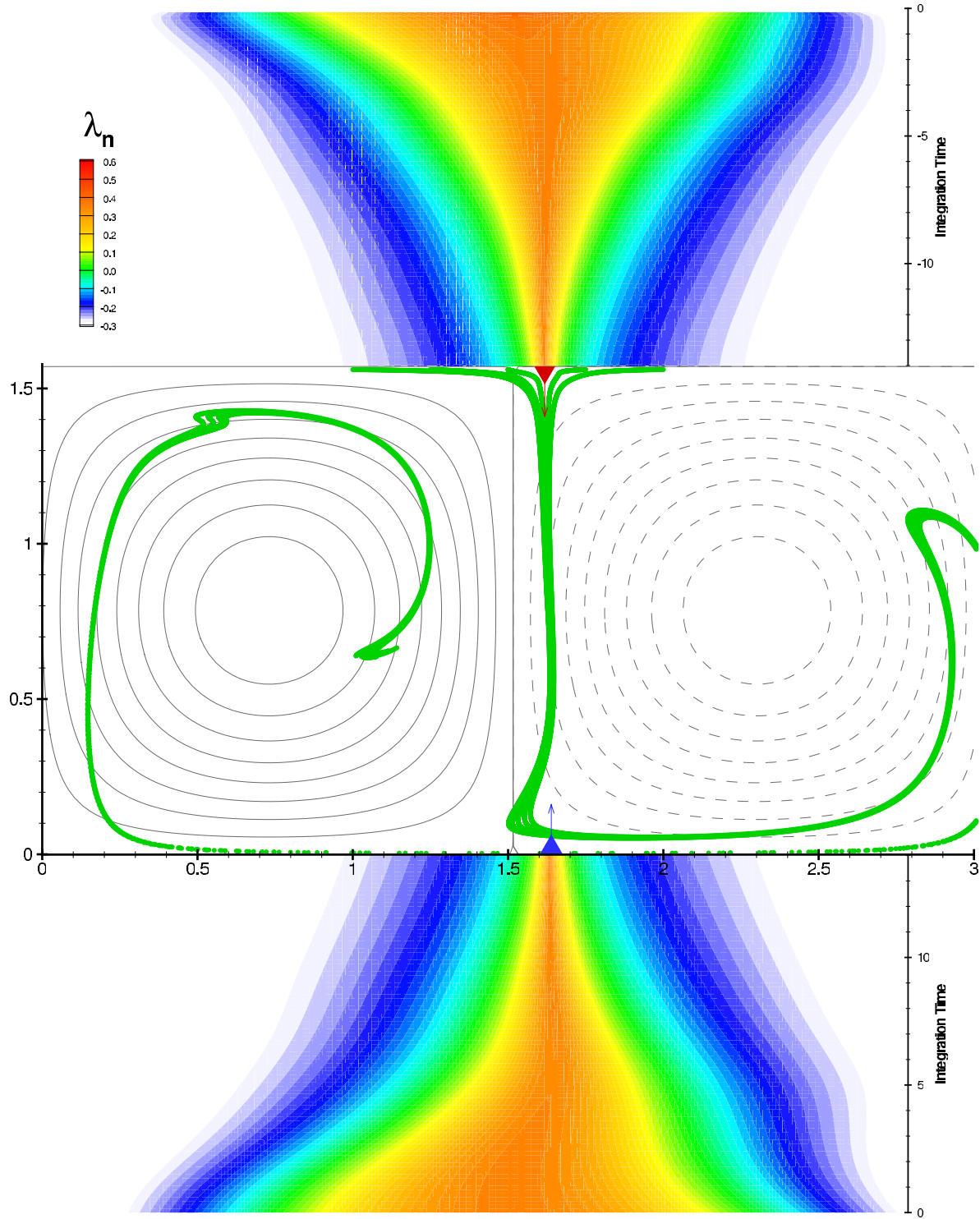


FIG. 8. (Color online) Transport in a chaotic Rayleigh-Bénard cell under random Gaussian forcing with amplitude  $B=0.48$  and decorrelation time  $\tau_0=\pi$ . Figures 6–8 show streamlines [Eq. (7) with  $A=0.18$  and  $k=2$ ], as well as separation and reattachment points at different times. Also shown are the  $\lambda_n$  fields in forward (below streamlines) and backward time (above streamlines). The color map is identical for the two  $\lambda_n$  plots and their maxima mark separation or reattachment. Particles (thick lines) released from five fixed locations near the top boundary confirm the predicted position and angle of separation. This panel corresponds to time  $t=60$ .

particles in Figs. 6–8 that corroborate the presence of separation and reattachment on the top and bottom cell boundaries at the predicted positions and angles. The particles are released continuously from five fixed locations right below the top boundary. The  $y$  coordinate of the release sites is  $\pi/2-2 \times 10^{-3}$ . The  $x$  coordinates of the release sites are 1.0,

1.25, 1.5, 1.75, and 2.0. As shown in Figs. 6–8, the advected particles converge toward the separation on the top boundary, then follow the separation profile inside the domain. To limit the number of rendered particles, they are followed for a maximum time  $\delta t=25$  after the release.

Figure 9 illustrates the robustness of separation and re-

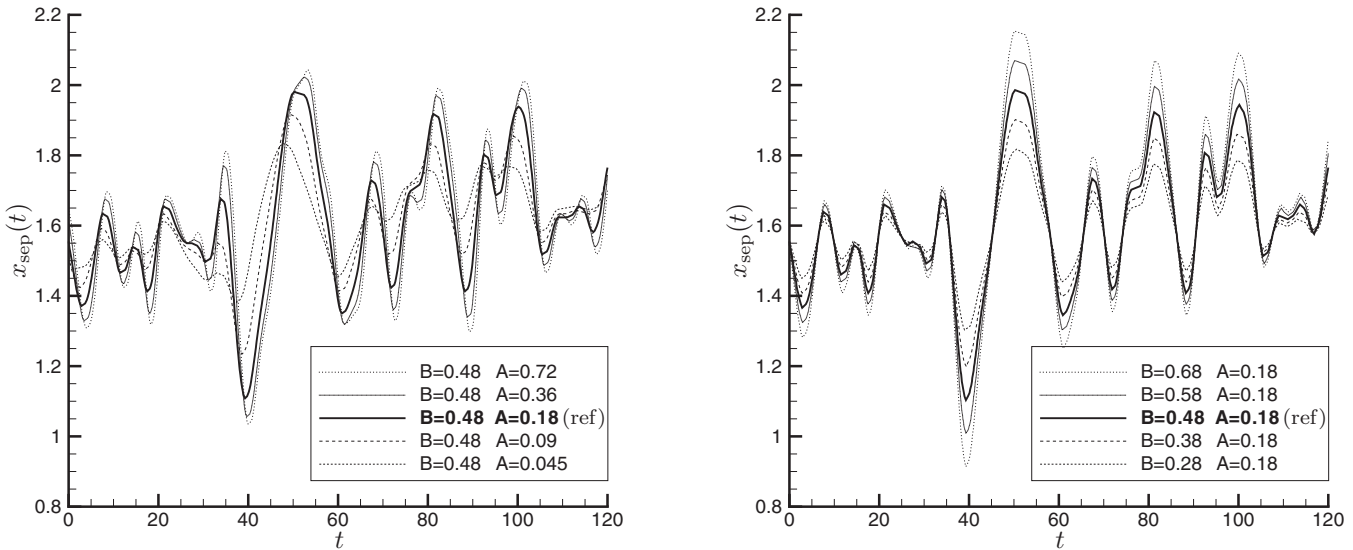


FIG. 9. Robustness of the separation point with respect to model parameters. Left panel: Influence of the maximum velocity  $A$ . Right panel: Influence of the amplitude of the lateral displacement  $B$ .

attachment detected by our criteria. We compute the separation point for various combinations of the parameters  $A$  (maximum vertical velocity) and  $B$  (variance of the lateral motion of the stagnation point). As seen in the figure, separation persists within a large range of the model parameters.

## VI. EXAMPLE 3: RANDOMLY OSCILLATING RAYLEIGH-BÉNARD CONVECTION WITH NOISE

Listed in items S3 and R3 of the separation and reattachment definitions, robustness with respect to perturbations of the flow field is required for observable separation or reattachment. Such robustness under changes of parameters follows from the structural stability of hyperbolic invariant manifolds.<sup>36</sup> A further practical question, however, is the robustness of separation and reattachment we locate under additional stochastic noise. The requirement of robustness under stochastic noise is stressed for features found in measured and simulated geophysical flow data.<sup>37</sup>

Assume that, instead of Eq. (2), the fluid particle motion satisfies

$$\dot{\mathbf{x}} = \mathbf{v}(\mathbf{x}, t) + \mathcal{N}(\mathbf{x}, t), \quad (10)$$

where  $\mathcal{N}$  is some noise superimposed on the velocity field. One might wonder whether separation points still exist for the perturbed system (10) and, if they do, how close a new separation point  $\mathbf{x}'_{\text{sep}}(t)$  is to its unperturbed counterpart  $\mathbf{x}_{\text{sep}}(t)$  identified for Eq. (2).

For the noise field  $\mathcal{N}$  in Eq. (10), we shall select  $\nabla \times \phi$ , where  $\phi$  is the realization of a multivariate Gaussian stream function noise. Such an unbiased noise field is characterized by its magnitude  $N$  and its covariance

$$\mathbf{E}[\phi(\mathbf{x}_1, t_1)\phi(\mathbf{x}_2, t_2)] = Ne^{-\|\mathbf{x}_1 - \mathbf{x}_2\|^2/\sigma^2 - |t_1 - t_2|^2/\tau^2}.$$

The parameters  $\sigma$  and  $\tau$  are commonly referred to as the decorrelation length and the decorrelation time of the signal, respectively. They determine the size and the time scale of the features in the noise field.<sup>38</sup>

Such a multivariate Gaussian noise field can be computed using the Wiener-Kitchine theorem and a three-dimensional version of Eq. (9). Level sets of streamfunction (7) superimposed with a realization of several noise fields are shown in Figs. 10 and 11. Note that both the background flow  $\mathbf{v}$  and the noise field  $\mathcal{N}$  satisfy the boundary condition at the horizontal boundaries; hence, the boundary conditions of the perturbed flow are unchanged.

Also note that several stagnation points are created by the noise on the top and bottom boundaries. The regular Eulerian pattern of Eq. (7) disappears and frequent and numerous bifurcations of stagnation points take place near the separation location. This shows that even simple flows with a small noise violate the stringent conditions of stagnation-point-based separation tracking algorithms that assume unique nonbifurcating stagnation points.

By contrast, our  $\lambda$ -criteria do not rely on instantaneous stagnation points and successfully capture separation in noisy flow fields. Indeed, Figs. 10 and 11 confirm that extrema of  $\lambda_n$  and  $\lambda_e$  continue to capture separation and reattachment under stochastic noise.

Figure 12 gives the position of the separation point at all times for each of the systems in Figs. 10 and 11. Note that our separation criteria involve integrals along trajectories. As a result, perturbations with relatively small time scales are rapidly averaged out when integrated. The position of the separation point is, therefore, only slightly affected by noise fields with small  $\tau$ , even when  $N$ , the amplitude of the noise, is large.

## VII. APPLICATION 1: ORTHOGONAL SEPARATION IN A QUASIGEOSTROPHIC MODEL OF THE NORTH ATLANTIC

Couillette and Wiggins<sup>8</sup> studied separation in a quasigeostrophic model of surface transport in the North Atlantic. Of primary interest is a separating trajectory on the Western boundary and its separation profile that propagates into the

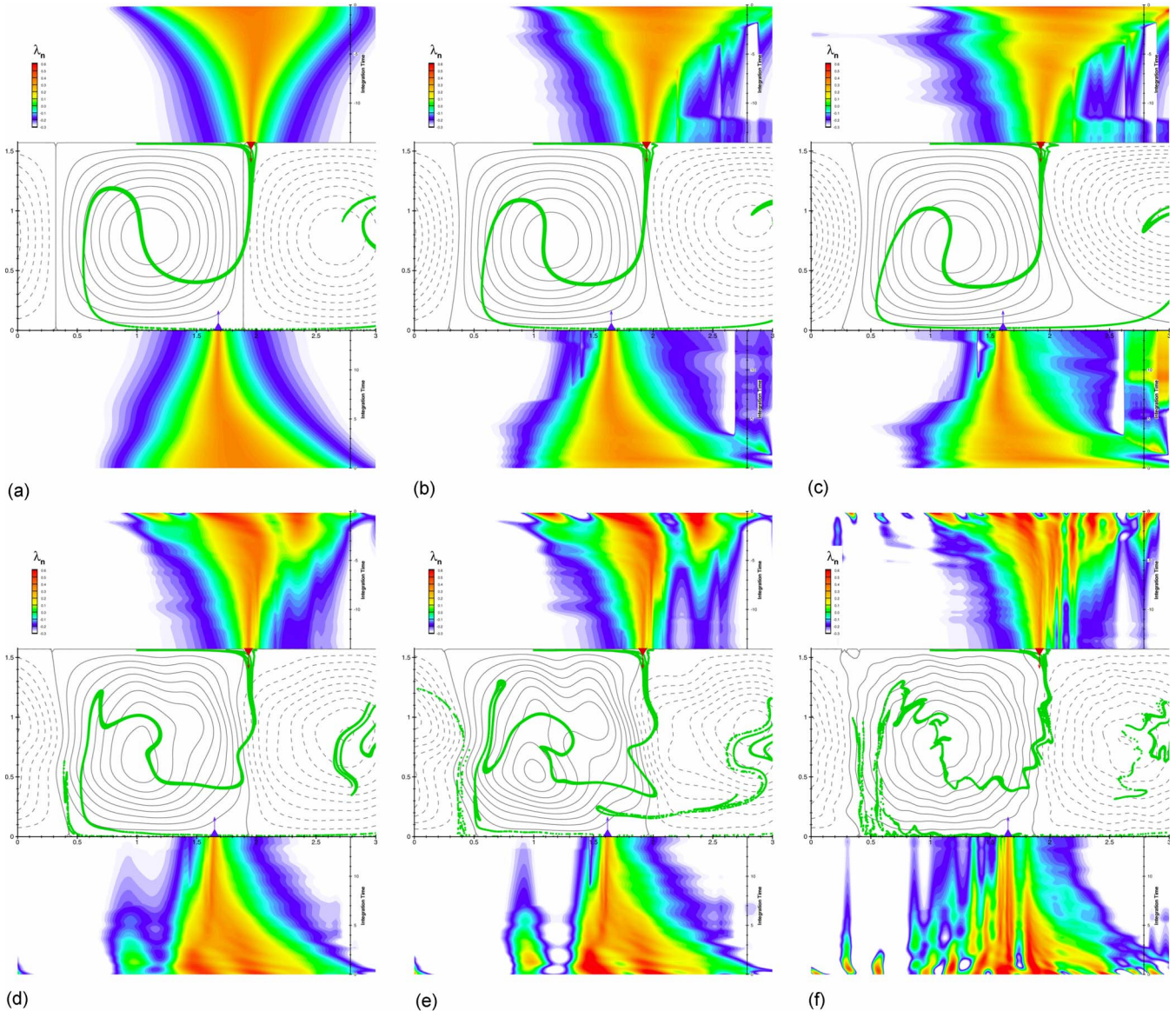


FIG. 10. (Color online) Transport in a chaotic noisy Rayleigh–Bénard cell using a random Gaussian forcing with amplitude  $B=0.48$  and decorrelation time  $\tau_0=\pi$ . Each panel shows the streamlines, separation, and reattachment points at time  $t=30.0$  for different noise fields  $\mathcal{N}$ . (a)  $N=0$ . (b)  $N=0.025$ ,  $\sigma=1$ ,  $\tau=\pi/10$ . (c)  $N=0.05$ ,  $\sigma=1$ ,  $\tau=\pi/10$ . (d)  $N=0.005$ ,  $\sigma=0.3$ ,  $\tau=\pi/10$ . (e)  $N=0.005$ ,  $\sigma=0.3$ ,  $\tau=\pi/2$ . (f)  $N=0.0015$ ,  $\sigma=0.1$ ,  $\tau=\pi/10$ . Particles (thick lines) released from five fixed locations on the top boundary validate the position and angle of the separation. Labels and color map are identical to those in Figs. 6–8 (enhanced online).

Gulf Stream. In the model used by Coulliette and Wiggins, there is always a slowly varying, isolated, stagnation point on the Western boundary. They find a separation point by integrating two (converging) trajectories that initially straddle the separation point. In the context of this smooth model, the hyperbolic trajectory computed by Coulliette and Wiggins corresponds to a separation point, as defined in this manuscript. The main advantage of the new method presented here is that it remains applicable when stagnation points bifurcate or get too close to one another.

In this manuscript, we also provide formula (4) for determining the angle at which the separation profile intersects the boundary. While unnoticed by Coulliette and Wiggins, all the separation profiles and reattachment profiles that they show are *orthogonal to the boundary*. Can we explain this property using formulas (4) and (6)?

The numerical results in Coulliette and Wiggins<sup>8</sup> are obtained using the model and the software of Rowley.<sup>27</sup> The latter provides options for simulating no-slip boundary conditions or no-stress boundary conditions. The simulations of Coulliette and Wiggins are therefore not only free slip (the normal component of the velocity vanishes:  $\langle \mathbf{v}, \mathbf{n} \rangle = 0$ ) but also incorporate the more constraining no-stress condition [the normal derivative of the tangential velocity vanishes:  $\langle \mathbf{e}, (\nabla \mathbf{v}) \mathbf{n} \rangle = 0$ ]. Since the Western boundary of the domain of Coulliette and Wiggins is a straight segment in a neighborhood of the separation point (i.e.,  $\mathbf{e}$  and  $\mathbf{n}$  are constant vectors), we also have  $\langle \mathbf{n}, (\nabla \mathbf{v}) \mathbf{e} \rangle = 0$ . Indeed, the velocity  $\mathbf{v}$  is oriented along the constant unit vector  $\mathbf{e}$ ; hence, its derivative in the normal direction must vanish.

Using  $\langle \mathbf{n}, (\nabla \mathbf{v}) \mathbf{e} \rangle = \langle \mathbf{e}, (\nabla \mathbf{v}) \mathbf{n} \rangle = 0$  in formula (4), we find

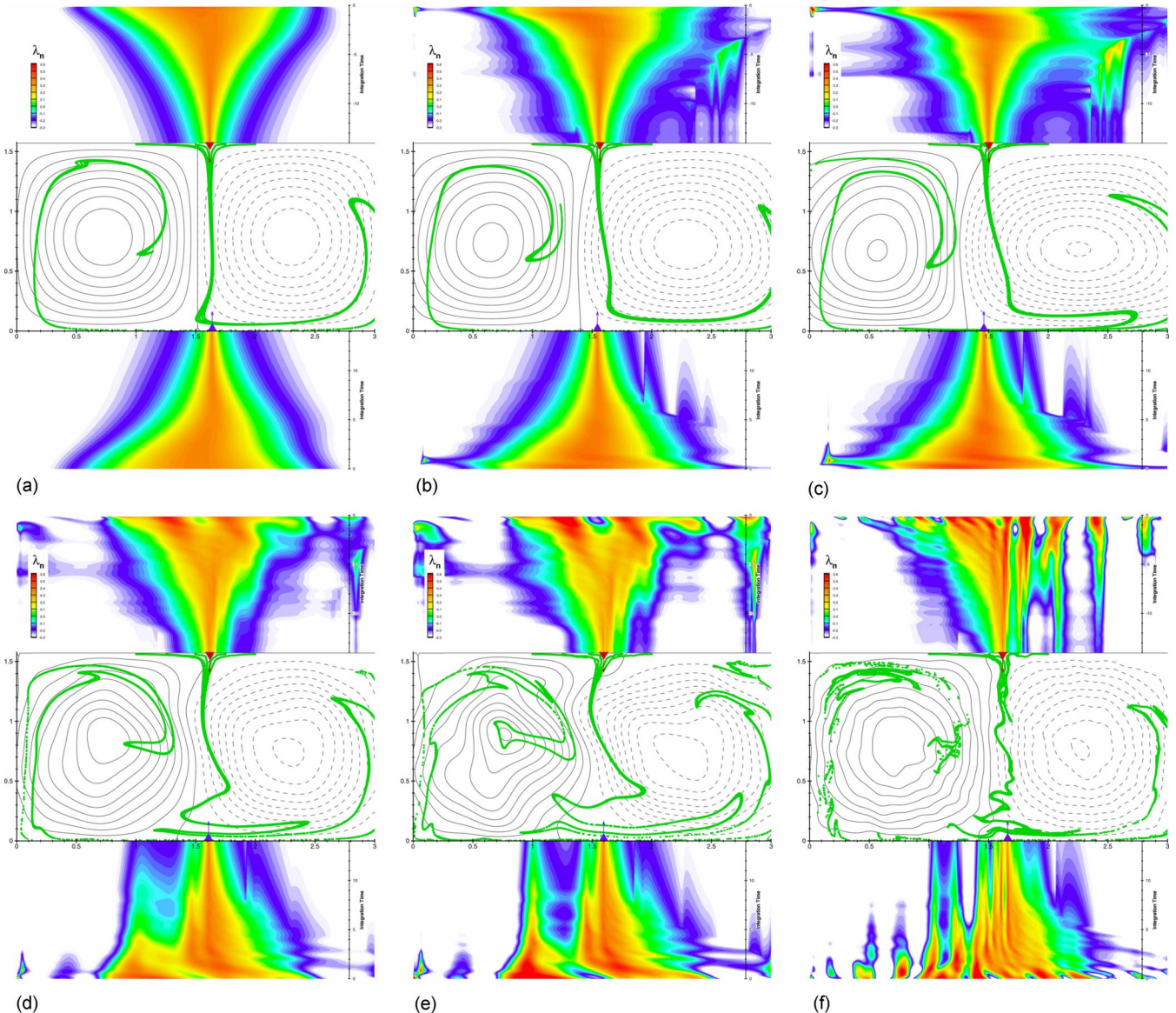


FIG. 11. (Color online) Transport in a chaotic noisy Rayleigh–Bénard cell using a random Gaussian forcing with amplitude  $B=0.48$  and decorrelation time  $\tau_0=\pi$ . Each panel shows the streamlines, separation, and reattachment points at time  $t=60.0$  for different noise fields  $\mathcal{N}$ . (a)  $N=0$ . (b)  $N=0.025$ ,  $\sigma=1$ ,  $\tau=\pi/10$ . (c)  $N=0.05$ ,  $\sigma=1$ ,  $\tau=\pi/10$ . (d)  $N=0.005$ ,  $\sigma=0.3$ ,  $\tau=\pi/10$ . (e)  $N=0.005$ ,  $\sigma=0.3$ ,  $\tau=\pi/2$ . (f)  $N=0.0015$ ,  $\sigma=0.1$ ,  $\tau=\pi/10$ . Particles (thick lines) released from five fixed locations on the top boundary validate the position and angle of the separation. Labels and color map are identical to those in Figs. 6–8 (enhanced online).

$$\cot \theta = 0 \Rightarrow \theta = \frac{\pi}{2}.$$

This shows that separation (and reattachment) in Coulliette and Wiggins<sup>8</sup> is necessarily orthogonal to the boundary. Whenever the stronger no-stress condition is used instead of free slip *and* the boundary is locally linear, separation and reattachment are constrained along directions that are orthogonal to the boundary.

### VIII. APPLICATION 2: BOUNDARY CURRENT SEPARATION AND REATTACHMENT IN MONTEREY BAY

In this section, we consider high-frequency (HF) radar measurements of surface currents  $\mathbf{v}(x, t)$  in Monterey Bay, CA.<sup>39,40</sup> We seek unsteady separation and reattachment along the coastline, which is treated as a free-slip boundary in ac-

cordance with common practice in geophysics. Indeed, large grid sizes typically do not allow for resolving the boundary layer flow in these systems. Separation and reattachment locations have a major impact on material transport in the bay determining, for instance, the spread of coastal pollution.<sup>7</sup>

Three HF radar antennas have been operating in Monterey Bay since 1994, collecting surface current measurements binned every hour on a horizontal uniform grid with  $1 \times 1 \text{ km}^2$  resolution.<sup>39,40</sup> Additional stations have been installed and will permit analysis along the entire California coastline. To apply our separation and reattachment criteria, we interpolate and extrapolate the available velocity data to obtain a smooth velocity field  $\mathbf{v}$  near the coastline. We require this processed velocity field to be everywhere tangent to the coastline and admit a continuous Jacobian along the coastline.

To obtain a velocity field  $\mathbf{v}$  satisfying the above require-

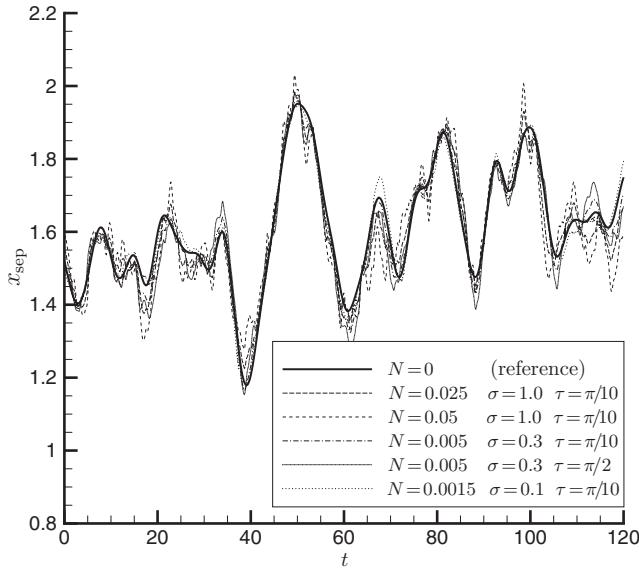


FIG. 12. Robustness of the separation point with respect to multivariate Gaussian noise.

ments, we use an extension of classic modal analysis to regions bounded by both a coastline (free-slip boundary condition) and an open boundary.<sup>41,42</sup> Specifically, we rely on a set of basis functions for velocity fields defined over the bay. The HF radar data are projected onto 64 of these modes, corresponding to length scales shorter than 2 km. The resulting nowcast of the surface velocity field is continuously differentiable and minimizes the least-squares difference with the measured currents.<sup>41,43</sup> Real-time measured currents as well as reconstructed velocity fields can be monitored online.<sup>44</sup>

If we assume that the density remains uniformly bounded from zero and from infinity along the boundary, the development in Appendix B implies that we do not need to compute both  $\lambda_n$  or  $\lambda_e$ . Indeed  $\lambda_n > 0 \Leftrightarrow \lambda_e < 0$ . Instead of selecting one of the two criteria, we prefer a hybrid, more robust, indicator:  $\lambda_n - \lambda_e$ . Note that in the (uncommon) case of a fluid where the density is unbounded or can approach zero, Appendix B would not apply. The function  $\lambda_n - \lambda_e$  could still be used to detect separation and reattachment, but each individual criterion would also have to be checked at the candidate separation points.

Figure 13 shows  $\lambda_n - \lambda_e$  as a function of time and of the arc length along the coastline for a fixed integration time  $T=48$  h, which matches the typical time scales observed by autonomous underwater vehicles in Monterey Bay.<sup>45</sup> Due to the temporal resolution of the data, peaks of uncertainties are expected within 2 h, which is more than 20 times shorter than the time scales of the dynamics in the bay and the finite integration time  $T$  used to compute our  $\lambda$ -criteria. Based on our numerical experiments in Sec. VI, the above ratio is expected to yield robust reattachment results.

Between August 1 and 6, 2003, there is one location at each time instance where  $\lambda_n - \lambda_e$  is positive. As predicted in Appendix B, similar plots with  $\lambda_n$  and  $\lambda_e$  alone (not shown, but similar to Fig. 13) reveal that this point satisfies both  $\lambda_n > 0$  and  $\lambda_e < 0$  and hence corresponds to a reattachment

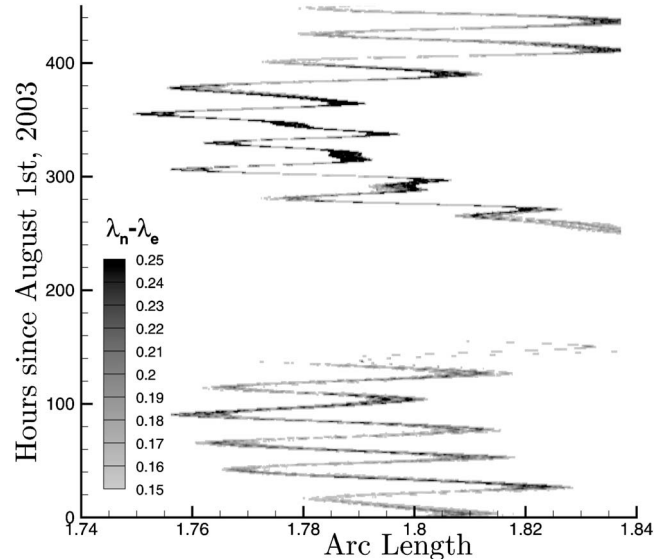


FIG. 13. Reattachment point in Monterey Bay. Highest level sets of  $\lambda_n - \lambda_e$  as a function of time and the arc length along the coastline.  $\lambda_n$  and  $\lambda_e$  are approximated using a finite integration time of  $T=48$  h. There is at most one reattachment point at each time, corresponding to a positive value of  $\lambda_n - \lambda_e$ .

point oscillating around the Monterey Peninsula until August 6 when it disappears (see Fig. 14). The reattachment point reappears on August 11 and persists for the entire month, briefly disappearing only between August 18 and 20.

Similarly, a plot of  $\lambda_n - \lambda_e$  in backward time reveals a moving separation point in the Northern part of the bay, near the city of Santa Cruz. During the month of August 2003, a single separation point is observed between August 8 and August 19, as well as after August 24. Note that the separation and reattachment points do not disappear during August: They move off our computational domain.

Figure 15 is a sketch of transport in Monterey Bay. It corresponds to a time when there is both a separation point and a reattachment point (i.e., between August 11 and 18, 2003 and between August 24 and 28, 2003). The corresponding separation and reattachment profiles are deduced from the streaklines of Fig. 14.

The separation and reattachment profiles in Fig. 15 occasionally approach each other but never intersect. The resulting thin channel between the two profiles is responsible for the continued ejection of fluid from the Bay toward the open ocean. This alleyway in the summer transport mechanism of Monterey Bay is consistent with the finite-time Lyapunov exponent plots based on the same radar data.<sup>7</sup> Recently, the existence of such a robust reattachment profile oscillating around the Monterey Peninsula was confirmed using the Harvard Ocean Prediction System and Error Subspace Statistical Estimation.<sup>37</sup>

We stress that the separation and reattachment points that we obtained for the bay cannot be inferred from instantaneous radar data. Specifically, stagnation points in the data bifurcate on hourly time scales and are often *absent* near actual fluid breakaway from the coast. When present, they are often accompanied by other instantaneous stagnation points that incorrectly signal local reattachment.

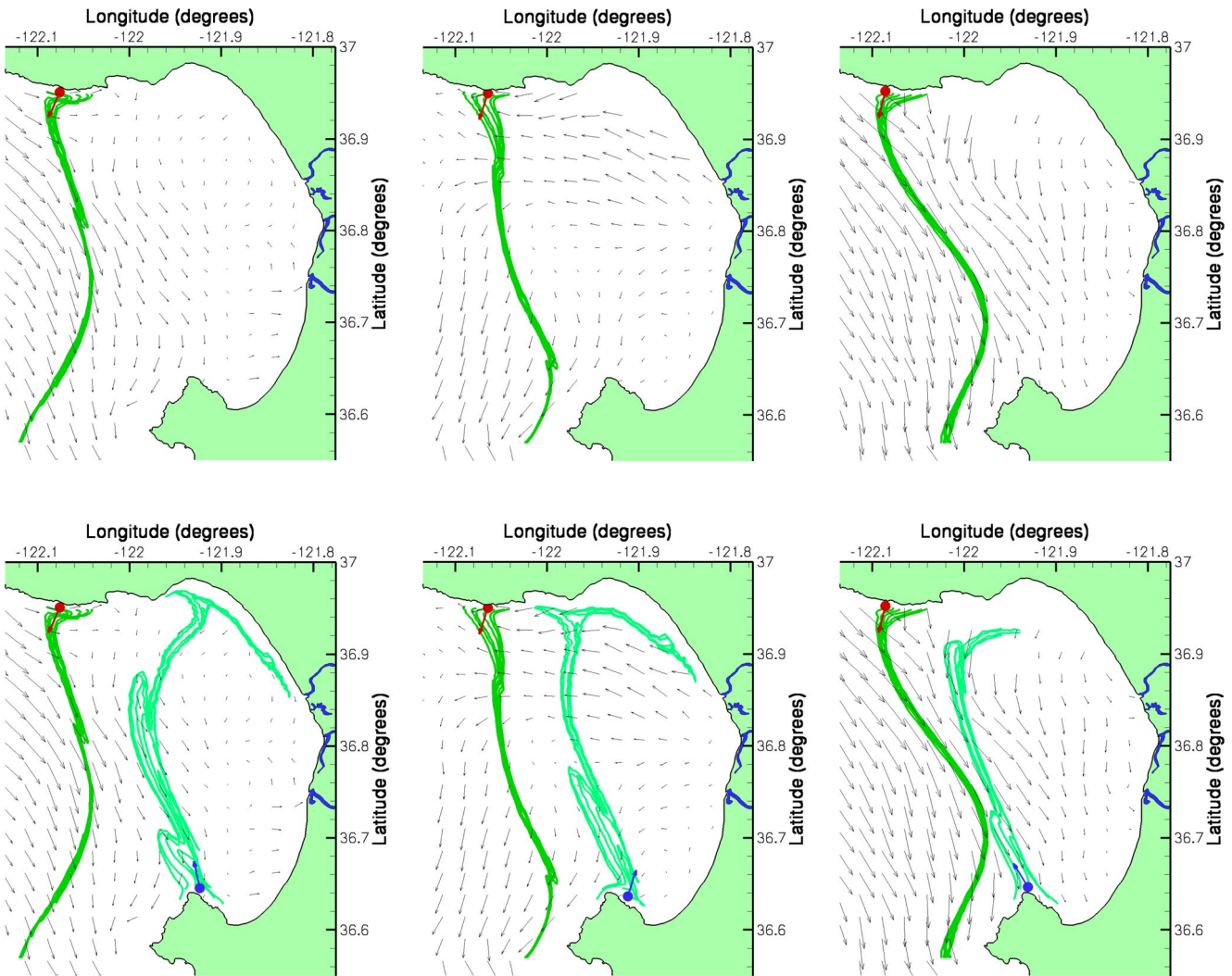


FIG. 14. (Color online) Separation and reattachment points in Monterey Bay. The upper panels show the separation point near Santa Cruz as well as streaklines released near the coast. The panels at the bottom show, in addition, the reattachment point and streamlines obtained from a backward-time integration. In this case, the base of the reattachment profile wanders around the Monterey Peninsula.

## IX. CONCLUSIONS

We have presented necessary and sufficient criteria for unsteady separation and reattachment for two-dimensional fluid flows with free-slip boundary conditions. Based on velocities and velocity derivatives along the boundary, our formulas predict Lagrangian separation location and angle. Only quantities on the boundary must be measured or modeled to use our criteria; they do not use interior information.

The Lagrangian view underlying our criteria differs from the traditional Eulerian view that considers instantaneous stagnation points as points of separation or make use of stagnation points to locate separation. Through examples, we have shown that the Lagrangian view is preferable, especially when several transient stagnation points evolve and bifurcate along the boundary; yet, no actual fluid breakaway is generated by most of them. Likewise, our criteria perform well in cases where separation occurs in the absence of persistent stagnation points. Furthermore, the theory and criteria

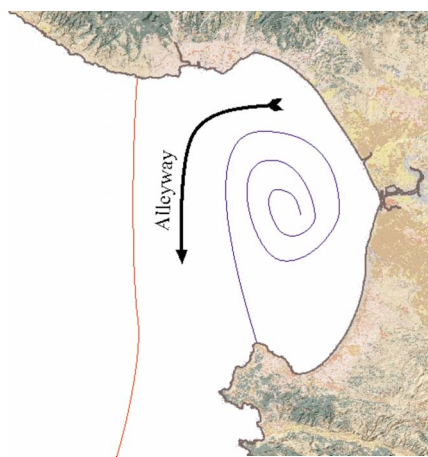


FIG. 15. (Color online) Sketch illustrating the geometry of transport in Monterey Bay based on the separation and reattachment profiles.

developed in this paper are Galilean invariant, unlike the notion of a stagnation point or a separating streamline.<sup>13</sup>

Fluid breakaway by itself does not guarantee large-scale separation: It may only be the indicator of the formation of a local separation bubble.<sup>6</sup> The ability of our theory to predict both of these phenomena is also its limitation: It is unable to differentiate between the two. Nevertheless, we stress that the objective of the free-slip model is to simulate a flow at low resolution: The boundary layer processes from the real flow (with a no-slip boundary) are averaged in few rows of grid points near the boundary which then looks like a slip surface. As a result, the free-slip separation points that we investigate in this paper should not be seen as confined to the boundary. They represent the global signature of complex boundary layer processes such as the ones depicted by Kormilas and Telionis.<sup>6</sup>

## ACKNOWLEDGMENTS

We are grateful to Chad Couillette and Naomi Leonard for their helpful remarks and enlightening discussions and we thank Damien Burch for pointing out that formula (A3) of Appendix A remains valid for time-dependent boundaries. We also thank Jeffrey Paduan, Michael Cook, and Daniel Atwater for their help with the HF radar data as well as for numerous discussions about transport in Monterey Bay. Separation and reattachment in Monterey Bay were computed with a modified version of MANGEN.<sup>46</sup> This work was supported by the Jules Revers Foundation, AFOSR Grant No. F49620-03-1-0200, NSF Grant No. DMS-04-04845, and ONR Grant Nos. N00014-02-1-0826 and N00014-04-1-0534.

## APPENDIX A: PROOF OF THE SLIP-SEPARATION CRITERION

### 1. Normal hyperbolicity

Based on the work of Fenichel<sup>36</sup> and Mañé,<sup>47</sup> *normal hyperbolicity* of a boundary trajectory  $\mathbf{x}(t)$ , with the stable (unstable) sub-bundle tangent to  $\mathcal{B}$ , is a sufficient and necessary condition for S1–S3 (for R1–R3). Thus, to locate separation or reattachment in the sense of S1–S3 (or R1–R3), it is sufficient to establish normal hyperbolicity for  $\mathbf{x}(t)$ . This appendix provides the details for separation; the same results in backward time identify reattachment.

The linearized flow along a boundary trajectory  $\mathbf{x}(t)$  is of the form

$$\dot{\xi} = \mathbf{A}(t)\xi, \quad \mathbf{A}(t) = \begin{pmatrix} u_x(\mathbf{x}(t), t) & u_y(\mathbf{x}(t), t) \\ v_x(\mathbf{x}(t), t) & v_y(\mathbf{x}(t), t) \end{pmatrix}, \quad (\text{A1})$$

with  $\xi(t) \in \mathbb{R}^2$  denoting an evolving infinitesimal perturbation to the trajectory  $\mathbf{x}(t)$ . Note that the proof remains valid for any other  $C^1$  orientable manifold since the equation of variations takes place in the tangent bundle.

At any boundary point  $\mathbf{x}$ , we introduce a local coordinate system whose axes are unit vectors parallel to the tangent vector  $\mathbf{e}(\mathbf{x}, t)$  and the normal vector  $\mathbf{n}(\mathbf{x}, t)$ . Specifically, we define the transformation matrix family  $\mathbf{T}(\mathbf{x}, t)$  as

$$\mathbf{T}(\mathbf{x}, t) = [\mathbf{e}(\mathbf{x}, t) \quad \mathbf{n}(\mathbf{x}, t)],$$

which we use to change the  $\xi$  coordinates along  $\mathbf{x}(t)$  to  $\mathbf{w}$  coordinates aligned with  $\mathbf{e}(\mathbf{x}(t), t)$  and  $\mathbf{n}(\mathbf{x}(t), t)$ . Such a coordinate change is defined by the relation

$$\xi = \mathbf{T}(\mathbf{x}(t), t)\mathbf{w}. \quad (\text{A2})$$

The coordinate change (A2) is similar to the transformation used to study Lagrangian coherent structures in slowly varying flows in Haller and Iacono.<sup>48</sup> It transforms the linearized flow (A1) into

$$\dot{\mathbf{w}} = \mathbf{B}(t)\mathbf{w}, \quad \mathbf{B}(t) = \begin{pmatrix} S_{\parallel}(t) & b(t) \\ 0 & S_{\perp}(t) \end{pmatrix}, \quad (\text{A3})$$

where

$$S_{\parallel}(t) = \langle \mathbf{e}, (\nabla \mathbf{v}) \mathbf{e} \rangle_{\mathbf{x}=\mathbf{x}(t)},$$

$$b(t) = [\langle \mathbf{e}, (\nabla \mathbf{v}) \mathbf{n} \rangle + \langle \mathbf{n}, (\nabla \mathbf{v}) \mathbf{e} \rangle]_{\mathbf{x}=\mathbf{x}(t)},$$

$$S_{\perp}(t) = \langle \mathbf{n}, (\nabla \mathbf{v}) \mathbf{n} \rangle_{\mathbf{x}=\mathbf{x}(t)}.$$

The brackets  $\langle \cdot, \cdot \rangle$  denote the inner product;  $S_{\parallel}(t)$  and  $S_{\perp}(t)$  are the tangential and normal rates of strain along the trajectory  $\mathbf{x}(t)$ . For incompressible flows, the identity  $S_{\parallel}(t) + S_{\perp}(t) = 0$  can be used to further simplify Eq. (A3).

The matrix representation of the linearized flow (A3) is upper diagonal and can therefore be solved explicitly. Direct integration gives the solution

$$\begin{aligned} \mathbf{w}(t; t_0) &= \Phi(t, t_0)\mathbf{w}_0, \quad \mathbf{w}_0 = \begin{pmatrix} w_{10} \\ w_{20} \end{pmatrix}, \\ \Phi(t, t_0) &= \begin{pmatrix} e^{\int_{t_0}^t S_{\parallel}(s) ds} & d(t, t_0) \\ 0 & e^{\int_{t_0}^t S_{\perp}(s) ds} \end{pmatrix}, \\ d(t, t_0) &= \int_{t_0}^t e^{\int_s^t S_{\parallel}(\tau) d\tau + \int_{t_0}^s S_{\perp}(\tau) d\tau} b(s) ds. \end{aligned} \quad (\text{A4})$$

Note that the line  $\{w_2=0\}$  is an invariant subspace for Eq. (A3) and hence for the flow map  $\Phi(t, t_0)$ . This invariant subspace is tangent to the boundary segment  $\mathcal{B}$  at  $\mathbf{x}(t)$ . The *a priori* knowledge of this invariant manifold is, in fact, the reason why we can solve Eq. (A4) explicitly.

Following Fenichel's theory,<sup>36</sup> the boundary segment  $\mathcal{B}$  is *normally hyperbolic* along  $\mathbf{x}(t)$  (with the stable sub-bundle aligned with the boundary and the unstable sub-bundle off the boundary) if

- (α) Any solution  $[w_1(t), 0]$  of Eq. (A3) decays to zero exponentially as  $t \rightarrow \infty$ ;
- (β) For any  $t \in \mathbb{R}$ , there exists a unique one-dimensional subspace,

$$\mathcal{N}^u(t) = \left\{ k \begin{pmatrix} w_1^0(t) \\ w_2^0(t) \end{pmatrix} \mid k \in \mathbb{R}, w_2^0(t) > 0, \quad \|(w_1^0(t), w_2^0(t))\| = 1 \right\},$$

such that for any for any initial time  $t_0$  and initial vec-

tor  $\mathbf{w}_0 \in \mathcal{N}^u(t_0)$ , we have  $\Phi(t, t_0)\mathbf{w}_0 \in \mathcal{N}^u(t)$  and  $\|\Phi(t, t_0)\mathbf{w}_0\|$  decays to zero exponentially as  $t \rightarrow -\infty$ .

Condition ( $\alpha$ ) ensures that infinitesimal perturbations to  $\mathbf{x}(t)$  along the boundary decay to zero exponentially. Condition ( $\beta$ ) guarantees that for any time  $t$ , there is an off-boundary direction (the separation direction) in which infinitesimal perturbations to  $\mathbf{x}(t)$  decay to zero in backward time. We show the geometry of conditions ( $\alpha$ ) and ( $\beta$ ) in Fig. 2.

## 2. Verifying normal hyperbolicity

Following Fenichel's theory<sup>36</sup> and using the explicit solution (A4), we restate property ( $\alpha$ ) as

$$\lambda_e = \limsup_{t \rightarrow -\infty} \frac{1}{t - t_0} \int_{t_0}^t S_{\parallel}(s) ds < 0. \quad (\text{A5})$$

Although formally dependent on the present time  $t_0$ , the Lyapunov-type number  $\lambda_e$  turns out to be constant in time along each trajectory.<sup>36</sup> To examine property ( $\beta$ ), we consider a time-dependent family of unit vectors  $\mathbf{r}^0(t)$  that are not tangent to the boundary  $\mathcal{B}$  at the point  $\mathbf{x}(t)$  at time  $t$ . Any such unit vector family can be written in the form

$$\mathbf{r}^0(t) = \begin{pmatrix} w_1^0(t) \\ w_2^0(t) \end{pmatrix} = \begin{pmatrix} \cos \theta(t) \\ \sin \theta(t) \end{pmatrix}, \quad \sin \theta(t) \neq 0.$$

The linearized flow along  $\mathbf{x}(t)$  advects the unit vector  $\mathbf{r}^0(t_0)$  into

$$\Phi(t, t_0)\mathbf{r}^0(t_0) = \begin{pmatrix} \cos \theta(t)e^{\int_{t_0}^t S_{\parallel}(s) ds} + \sin \theta(t_0)d(t, t_0) \\ \sin \theta(t_0)e^{\int_{t_0}^t S_{\perp}(s) ds} \end{pmatrix}, \quad (\text{A6})$$

whose angle  $\theta(t)$  with the boundary satisfies

$$\begin{aligned} & [\cos \theta(t_0)e^{\int_{t_0}^t S_{\parallel}(s) ds} + \sin \theta(t_0)d(t, t_0)] \\ &= \cot \theta(t) [\sin \theta(t_0)e^{\int_{t_0}^t S_{\perp}(s) ds}]. \end{aligned} \quad (\text{A7})$$

Using Eq. (A6), property ( $\beta$ ) can be succinctly expressed as

$$\lambda_n = \liminf_{t \rightarrow -\infty} \frac{1}{t - t_0} \ln \|\Phi(t, t_0)\mathbf{r}^0(t_0)\| > 0,$$

where  $\lambda_n$  refers to the unstable Lyapunov-type number introduced by Fenichel,<sup>36</sup> evaluated in the present context. By Eq. (A7), the norm of  $\Phi(t, t_0)\mathbf{r}^0(t_0)$  can be written as

$$\begin{aligned} \|\Phi(t, t_0)\mathbf{r}^0(t_0)\| &= \sqrt{[\cos \theta(t_0)e^{\int_{t_0}^t S_{\parallel}(s) ds} + \sin \theta(t_0)d(t, t_0)]^2 + [\sin \theta(t_0)e^{\int_{t_0}^t S_{\perp}(s) ds}]^2} \\ &= \left| \sqrt{1 + \cot^2 \theta(t)} \sin \theta(t_0)e^{\int_{t_0}^t S_{\perp}(s) ds} \right|. \end{aligned} \quad (\text{A8})$$

Therefore, since

$$\limsup_{t \rightarrow -\infty} |\cot \theta(t)| < \infty, \quad (\text{A9})$$

and  $\sin \theta(t_0) \neq 0$  by S2, then (A8) is equivalent to

$$\begin{aligned} \lambda_n &= \liminf_{t \rightarrow -\infty} \frac{1}{t - t_0} \ln \left| \sqrt{1 + \cot^2 \theta(t)} \sin \theta(t_0)e^{\int_{t_0}^t S_{\perp}(s) ds} \right| \\ &= \liminf_{t \rightarrow -\infty} \frac{1}{t - t_0} \int_{t_0}^t S_{\perp}(s) ds. \end{aligned}$$

Consequently, condition (A9) and properties (2) and (3) can be expressed as

$$\begin{aligned} \lambda_e &= \limsup_{t \rightarrow -\infty} \frac{1}{t - t_0} \int_{t_0}^t S_{\parallel}(s) ds < 0, \\ \lambda_n &= \liminf_{t \rightarrow -\infty} \frac{1}{t - t_0} \int_{t_0}^t S_{\perp}(s) ds > 0, \\ \limsup_{t \rightarrow -\infty} |\cot \theta(t)| &< \infty. \end{aligned} \quad (\text{A10})$$

The last condition in Eq. (A10) can be formulated in a simpler form. Observe that Eq. (A7) implies

$$\cot \theta(t) = \cot \theta(t_0)e^{\int_{t_0}^t [S_{\parallel}(s) - S_{\perp}(s)] ds} + d(t, t_0)e^{-\int_{t_0}^t S_{\perp}(s) ds}.$$

Thus, the third condition in Eq. (A10) is equivalent to the existence of two constants  $K_1, K_2 > 0$  such that for  $t_0 - t$  large enough,

$$K_1 \leq |\cot \theta(t_0)e^{\int_{t_0}^t [S_{\parallel}(s) - S_{\perp}(s)] ds} + d(t, t_0)e^{-\int_{t_0}^t S_{\perp}(s) ds}| \leq K_2.$$

Dividing this inequality by  $e^{\int_{t_0}^t [S_{\parallel}(s) - S_{\perp}(s)] ds}$  gives

$$\begin{aligned} \frac{K_1}{e^{\int_{t_0}^t [S_{\parallel}(s) - S_{\perp}(s)] ds}} &\leq |\cot \theta(t_0) + d(t, t_0)e^{-\int_{t_0}^t S_{\parallel}(s) ds}| \\ &\leq \frac{K_2}{e^{\int_{t_0}^t [S_{\parallel}(s) - S_{\perp}(s)] ds}}. \end{aligned} \quad (\text{A11})$$

Taking the limit for  $t \rightarrow -\infty$  in Eq. (A11), using the first two conditions in Eq. (A10), and recalling the definition of  $d(t, t_0)$  from Eq. (A4), we find that Eq. (A11) implies

$$\begin{aligned} \lim_{t \rightarrow -\infty} & \left[ \cot \theta(t_0) + e^{-\int_{t_0}^t S_{\parallel}(s) ds} \int_{t_0}^t e^{(\int_s^t S_{\parallel}(\tau) d\tau + \int_{t_0}^s S_{\perp}(\tau) d\tau)} b(s) ds \right] \\ &= 0, \end{aligned} \quad (\text{A12})$$

which is equivalent to

$$\cot \theta(t_0) = - \lim_{t \rightarrow -\infty} \int_{t_0}^t e^{(f_s^{t_0} S_{||}(\tau) d\tau + f_{t_0}^s S_{\perp}(\tau) d\tau)} b(s) ds. \quad (\text{A13})$$

As a result, the last condition in Eq. (A10) is equivalent to

$$|\cot \theta(t_0)| = \left| \lim_{t \rightarrow -\infty} \int_{t_0}^t e^{[f_s^{t_0} [S_{||}(\tau) - S_{\perp}(\tau)] d\tau]} b(s) ds \right| < \infty \quad (\text{A14})$$

for all  $t_0$ .

Note, however, that the continuous differentiability of  $\mathbf{v}$  and the compactness of  $\mathcal{B}$  imply that  $b(s)$  is uniformly bounded. Therefore, by the first two conditions in Eq. (A10), the improper integral in Eq. (A14) converges. As a result, the last condition in Eq. (A10) follows from the first two conditions.

After the substitution of  $t-T$  for  $t$  and  $t$  for  $t_0$ , the computations above show that the separation criterion (3) is necessary and that the separation angle is given by formula (4). The criterion is also necessary, as shown by Mañé.<sup>47</sup> Reversing the direction of time in our arguments, we obtain the reattachment criterion (5) and the reattachment angle formula (6).

### 3. Remarks about normal hyperbolicity and the separation problem

We close with two remarks on subtle modifications to the normally hyperbolic invariant manifold results of Fenichel that are needed before the results apply in the present context. First, according to Fenichel's results, the  $\limsup$  in Eq. (A5) would have to be taken as  $t \rightarrow +\infty$ , not as  $t \rightarrow -\infty$ . The reason is Fenichel's existence proof for a stable manifold to  $\mathbf{x}(t)$ , which builds on asymptotic properties of nearby solutions in the  $t \rightarrow +\infty$  limit.

In our specific context, however, the boundary segment  $\mathcal{B}$  is known to be an invariant manifold for the velocity field  $\mathbf{v}$ . Within this invariant manifold, a neighborhood of  $\mathbf{x}(t)$  acts as a stable manifold for  $\mathbf{x}(t)$  (based on velocity data up to the present time  $t_0$ ) by the first condition in Eq. (A10). As a result, a separate existence proof for a stable manifold of  $\mathbf{x}(t)$  is not needed.

Second, Fenichel's original results apply to compact invariant manifolds in autonomous (i.e., time independent) vector fields. The velocity field  $\mathbf{v}(\mathbf{x}, t)$  used here becomes autonomous only on the extended phase space  $\{(\mathbf{x}, t) | \mathbf{x} \in \Omega, t \in \mathbb{R}\}$ , on which the extended trajectory  $(\mathbf{x}(t), t)$  is *not* compact.

Nevertheless, Fenichel's proof carries over to the non-compact case as long as the Lyapunov-type numbers  $\lambda_e$  and  $\lambda_n$  within the invariant manifold in question are uniformly

bounded away from zero, and  $\mathbf{v}$  and its first derivatives are uniformly bounded in time. Here, the invariant manifold to be studied is the single extended trajectory  $\{(\mathbf{x}(t), t) | t \in \mathbb{R}\}$ ; thus, Eq. (A10) ensures the uniform boundedness of Lyapunov-type numbers from zero along the manifold. As for the uniform boundedness of  $\mathbf{v}$  and its derivatives, that is an explicit assumption in Sec. II. With these observations, Fenichel's proofs carry over to the noncompact manifold  $(\mathbf{x}(t), t)$ .

## APPENDIX B: SIMPLIFIED CRITERIA FOR FLUIDS WITH BOUNDED DENSITY

Two conditions are necessary to satisfy the separation criterion (3). For incompressible flows, one implies the other. The equivalence between the two conditions remains true for any flow which has a density  $\rho$  that remains bounded (away from infinity) and uniformly bounded away from 0, which we prove in this appendix. This observation simplifies the separation criterion considerably as, for most fluids, only one of  $\lambda_e$  or  $\lambda_n$  must be computed.

Let us suppose that the first condition,

$$\lambda_e(t) = \limsup_{T \rightarrow +\infty} \frac{1}{T} \int_{t-T}^t \langle \mathbf{e}, (\nabla \mathbf{v}) \mathbf{e} \rangle_{[\mathbf{x}(s), s]} ds < 0,$$

is satisfied and that the density  $\rho$  satisfies

$$\exists k_{\min}, k_{\max} > 0: \quad \forall \mathbf{x} \in \Omega: \quad \forall t \in \mathbb{R}: \quad$$

$$\rho(\mathbf{x}, t) < k_{\max} \quad \text{and} \quad \rho(\mathbf{x}, t) > k_{\min}.$$

We want to show that this necessarily implies the second condition

$$\lambda_n(t) = \liminf_{T \rightarrow +\infty} \frac{1}{T} \int_{t-T}^t \langle \mathbf{n}, (\nabla \mathbf{v}) \mathbf{n} \rangle_{[\mathbf{x}(s), s]} ds > 0.$$

To prove this result, note that the continuity equation states  $d\rho/dt = -\rho \nabla \cdot \mathbf{v}$ . Integrating this equation along a boundary trajectory from time  $t-T$  to time  $t$ , we get

$$\begin{aligned} \ln \rho[\mathbf{x}(t), t] - \ln \rho[\mathbf{x}(t-T), t-T] &= - \int_{t-T}^t (\nabla \cdot \mathbf{v})_{[\mathbf{x}(s), s]} ds \\ &= - \int_{t-T}^t [\langle \mathbf{e}, (\nabla \mathbf{v}) \mathbf{e} \rangle_{[\mathbf{x}(s), s]} + \langle \mathbf{n}, (\nabla \mathbf{v}) \mathbf{n} \rangle_{[\mathbf{x}(s), s]}] ds \end{aligned}$$

Let us fix  $t$ . If the density  $\rho[\mathbf{x}(t-T), t-T]$  is to remain uniformly bounded away from infinity and from zero, when  $T \rightarrow +\infty$ , we must have

$$\begin{aligned} \liminf_{T \rightarrow +\infty} \left| \int_{t-T}^t [\langle \mathbf{e}, (\nabla \mathbf{v}) \mathbf{e} \rangle_{[\mathbf{x}(s), s]} + \langle \mathbf{n}, (\nabla \mathbf{v}) \mathbf{n} \rangle_{[\mathbf{x}(s), s]}] ds \right| &< +\infty, \\ \Rightarrow \liminf_{T \rightarrow +\infty} \frac{1}{T} \left| \int_{t-T}^t [\langle \mathbf{e}, (\nabla \mathbf{v}) \mathbf{e} \rangle_{[\mathbf{x}(s), s]} + \langle \mathbf{n}, (\nabla \mathbf{v}) \mathbf{n} \rangle_{[\mathbf{x}(s), s]}] ds \right| &= 0. \end{aligned} \quad (\text{B1})$$

We can now prove that one condition implies the other by contradiction. Let us assume that we have  $\lambda_e < 0$  and, at the same time,  $\lambda_n \leq 0$ . This would imply

$$\begin{aligned} \liminf_{T \rightarrow +\infty} \frac{1}{T} \int_{t-T}^t \langle \mathbf{e}, (\nabla \mathbf{v}) \mathbf{e} \rangle_{[\mathbf{x}(s), s]} ds \\ \leq \limsup_{T \rightarrow +\infty} \frac{1}{T} \int_{t-T}^t \langle \mathbf{e}, (\nabla \mathbf{v}) \mathbf{e} \rangle_{[\mathbf{x}(s), s]} ds = \lambda_e < 0 \end{aligned}$$

and

$$\liminf_{T \rightarrow +\infty} \frac{1}{T} \int_{t-T}^t \langle \mathbf{n}, (\nabla \mathbf{v}) \mathbf{n} \rangle_{[\mathbf{x}(s), s]} ds = \lambda_n \leq 0,$$

which leads to

$$\liminf_{T \rightarrow +\infty} \frac{1}{T} \int_{t-T}^t (\langle \mathbf{e}, (\nabla \mathbf{v}) \mathbf{e} \rangle_{[\mathbf{x}(s), s]} + \langle \mathbf{n}, (\nabla \mathbf{v}) \mathbf{n} \rangle_{[\mathbf{x}(s), s]}) ds < 0,$$

and contradicts Eq. (B1).

As a result we have shown that provided that the density  $\rho[\mathbf{x}(t-T), t-T]$  remains uniformly bounded from zero and infinity for  $T \rightarrow +\infty$ ,  $\lambda_e < 0 \Rightarrow \lambda_n > 0$ . A similar development can be used to prove the reverse statement:  $\lambda_n > 0 \Rightarrow \lambda_e < 0$ . The same conclusion holds for reattachment.

- <sup>1</sup>L. Prandtl, *Über Flüssigkeitsbewegungen bei sehr kleiner Reibung* (Verh. II Int. Math.-Kongr., Heidelberg, 1904).
- <sup>2</sup>N. Rott, "Diffraction of a weak shock with vortex generation," *J. Fluid Mech.* **1**, 111 (1956).
- <sup>3</sup>W. R. Sears and D. P. Telionis, "Boundary-layer separation in unsteady flows," *SIAM J. Appl. Math.* **28**, 215 (1975).
- <sup>4</sup>L. L. Van Dommelen and S. F. Shen, "The spontaneous generation of the singularity in a separating laminar boundary layer," *J. Comput. Phys.* **38**, 125 (1980).
- <sup>5</sup>G. Haller, "Exact theory of unsteady separation for two-dimensional flows," *J. Fluid Mech.* **512**, 257 (2004).
- <sup>6</sup>C. A. Koromikas and D. P. Telionis, "Unsteady laminar separation: An experimental study," *J. Fluid Mech.* **97**, 347 (1980).
- <sup>7</sup>C. Coulibbie, F. Lekien, G. Haller, J. Paduan, and J. E. Marsden, "Optimal pollution mitigation in Monterey Bay based on coastal radar data and nonlinear dynamics," *Environ. Sci. Technol.* **41**, 6562 (2007).
- <sup>8</sup>C. Coulibbie and S. Wiggins, "Intergyre transport in a wind-driven, quasi-geostrophic double gyre: An application of lobe dynamics," *Nonlinear Processes Geophys.* **8**, 69 (2001).
- <sup>9</sup>M. Ghil, T. Ma, and S. Wang, "Structural bifurcation of 2-d incompressible flows," *Indiana Univ. Math. J.* **50**, 159 (2001).
- <sup>10</sup>K. Ide, D. Small, and S. Wiggins, "Distinguished hyperbolic trajectories in time-dependent fluid flows: Analytical and computational approach for velocity fields defined as data sets," *Nonlinear Processes Geophys.* **9**, 237 (2002).
- <sup>11</sup>A. M. Mancho, D. Small, and S. Wiggins, "Computation of hyperbolic trajectories and their stable and unstable manifolds for oceanographic flows represented as data sets," *Nonlinear Processes Geophys.* **11**, 17 (2004).
- <sup>12</sup>G. Haller and A. Poje, "Finite-time transport in aperiodic flows," *Physica D* **119**, 352 (1998).
- <sup>13</sup>F. Lekien and C. Coulibbie, "Chaotic stirring in quasi-turbulent flows," *Philos. Trans. R. Soc. London, Ser. A* **365**, 3061 (2007).
- <sup>14</sup>S. C. Shadden, F. Lekien, and J. E. Marsden, "Definition and properties of Lagrangian coherent structures from finite-time Lyapunov exponents in two-dimensional aperiodic flows," *Physica D* **212**, 271 (2005).
- <sup>15</sup>F. Lekien, C. Coulibbie, A. J. Mariano, E. H. Ryan, L. K. Shay, G. Haller, and J. E. Marsden, "Pollution release tied to invariant manifolds: A case study for the coast of Florida," *Physica D* **210**, 1 (2005).
- <sup>16</sup>E. P. Chassignet and P. R. Gent, "The influence of boundary conditions on mid-latitude jet separation in ocean numerical models," *J. Phys. Oceanogr.* **21**, 1290 (1991).
- <sup>17</sup>D. P. Marshall and C. E. Tansley, "An implicit formula for boundary current separation," *J. Phys. Oceanogr.* **31**, 1633 (2001).
- <sup>18</sup>M. J. Olascoaga, I. I. Rypina, M. G. Brown, F. J. Beron-Vera, H. Kocak, L. E. Brand, G. R. Halliwell, and L. K. Shay, "Persistent transport barrier on the West Florida Shelf," *Geophys. Res. Lett.* **33**, L22603, DOI: 10.1029/2006GL027800 (2006).
- <sup>19</sup>D. S. Dandy and L. G. Leal, "Boundary-layer separation from a smooth slip surface," *Phys. Fluids* **29**, 1360 (1986).
- <sup>20</sup>H. A. Stone, "An interpretation of the translation of drops and bubbles at high Reynolds numbers in terms of the vorticity field," *Phys. Fluids A* **5**, 2567 (1993).
- <sup>21</sup>J. F. Peng, J. O. Dabiri, P. G. Madden, and G. V. Lauder, "Non-invasive measurement of instantaneous forces during aquatic locomotion: A case study of the bluegill sunfish pectoral fin," *J. Exp. Biol.* **210**, 685 (2007).
- <sup>22</sup>A. Beskok, "Validation of new velocity-slip model for separated gas microflows," *Numer. Heat Transfer, Part B* **40**, 451 (2001).
- <sup>23</sup>H. Xue, B. Xu, Y. Wei, and J. Wu, "Unique behaviors of a backward-facing step flow at microscale," *Numer. Heat Transfer, Part B* **47**, 251 (2005).
- <sup>24</sup>R. B. Srygley and A. R. L. Thomas, "Unconventional lift-generating mechanisms in free-flying butterflies," *Nature (London)* **420**, 660 (2002).
- <sup>25</sup>T. H. Solomon and J. P. Gollub, "Passive transport in steady Rayleigh-Bénard convection," *Phys. Fluids* **31**, 1372 (1988).
- <sup>26</sup>V. Rom-Kedar, "Transport rates of a class of two-dimensional maps and flows," *Physica D* **43**, 229 (1990).
- <sup>27</sup>C. A. Rowley, "A modeling study of the North Atlantic current," Ph.D thesis, University of Rhode Island (1996).
- <sup>28</sup>R. Camassa, and S. Wiggins, "Chaotic advection in a Rayleigh-Bénard flow," *Phys. Rev. A* **43**, 774 (1991).
- <sup>29</sup>G. Haller, "Finding finite-time invariant manifolds in two-dimensional velocity fields," *Chaos* **10**, 99 (2000).
- <sup>30</sup>F. Lekien, S. C. Shadden, and J. E. Marsden, "Lagrangian coherent structures in n-dimensional systems," *J. Math. Phys.* **48**, 065404 (2007).
- <sup>31</sup>T. H. Solomon and J. P. Gollub, "Sheared boundary-layers in turbulent Rayleigh-Bénard convection," *Phys. Rev. Lett.* **64**, 2382 (1990).
- <sup>32</sup>T. H. Solomon and J. P. Gollub, "Thermal-boundary layers and heat-flux in turbulent convection—The role of recirculating-flows," *Phys. Rev. A* **43**, 6683 (1991).
- <sup>33</sup>T. H. Solomon and J. P. Gollub, "Chaotic particle-transport in time-dependent Rayleigh-Bénard convection," *Phys. Rev. A* **38**, 6280 (1988).
- <sup>34</sup>C. L. Nikias and A. P. Petropulu, *Higher-order Spectra Analysis*, Signal Processing Series (Prentice Hall, Englewood Cliffs, NJ, 1993).
- <sup>35</sup>The C/C++ version of the multivariate Gaussian noise generator can be downloaded at <http://www.lekien.com/~francois/software/rndfieldgen>. A Matlab version is also available from Olaf Arie Cirpka at [http://matlabdb.mathematik.uni-stuttgart.de/download.jsp?MP\\_ID=31](http://matlabdb.mathematik.uni-stuttgart.de/download.jsp?MP_ID=31) (maximum three dimensions).
- <sup>36</sup>N. Fenichel, "Persistence and smoothness of invariant manifolds for flows," *Indiana Univ. Math. J.* **21**, 193 (1971).
- <sup>37</sup>P. F. J. Lermusiaux, C.-S. Chiu, G. C. Gawarkiewicz, P. Abbot, A. R. Robinson, P. J. Haley, P. J. Leslie, S. J. Majumdar, A. Pang, and F. Lekien, "Quantifying uncertainties in ocean predictions," *Oceanogr.* **19**, 80 (2006).
- <sup>38</sup>H. J. Thiebaut, "Experiment with correlation representations for objective analysis," *Mon. Weather Rev.* **103**, 617 (1975).
- <sup>39</sup>J. D. Paduan and M. S. Cook, "Mapping surface currents in Monterey Bay with CODAR-type HR radar," *Oceanogr.* **10**, 49 (1997).
- <sup>40</sup>J. D. Paduan and L. K. Rosenfeld, "Remotely sensed surface currents in Monterey Bay from shore-based HF radar (coastal ocean dynamics application radar)," *J. Geophys. Res., [Oceans]* **101**, 20669, DOI: 10.1029/96JC01663 (1996).
- <sup>41</sup>F. Lekien, C. Coulibbie, R. Bank, and J. Marsden, "Open-boundary modal analysis: Interpolation, extrapolation, and filtering," *J. Geophys. Res., [Oceans]* **109**, C12004, DOI: 10.1029/2004JC002323 (2004).
- <sup>42</sup>B. L. Lipphardt, Jr., A. D. Kirwan, Jr., C. E. Grosch, J. K. Lewis, and J. D. Paduan, "Blending HF radar and model velocities in Monterey Bay through normal mode analysis," *J. Geophys. Res., [Oceans]* **105**, 3425, DOI: 10.1029/1999JC00295 (2000).

- <sup>43</sup>D. M. Kaplan and F. Lekien, "Spatial interpolation and filtering of surface current data based on open-boundary modal analysis," *J. Geophys. Res., [Oceans]* **112** C12007, DOI: 10.1029/2006JC003984 (2007).
- <sup>44</sup>Real-time measured currents and reconstructed surface fields can be monitored at <http://www.mangen.org/realtime>.
- <sup>45</sup>D. L. Rudnick, R. E. Davis, C. C. Eriksen, D. M. Frantoni, and M. J. Perry, "Underwater gliders for ocean research," *Mar. Technol. Soc. J.* **38**, 48 (2004).

<sup>46</sup>MANGEN is a computer software for studying nonlinear dynamics and Lagrangian coherent structures in dynamical systems defined as 2D+1 dataset (MANGEN is available at <http://www.lekien.com/~francois/software/mangen>).

<sup>47</sup>R. Mañé, "Persistent manifolds are normally hyperbolic," *Trans. Am. Math. Soc.* **246**, 261 (1978).

<sup>48</sup>G. Haller and R. Iacono, "Stretching, alignment, and shear in slowly varying velocity fields," *Phys. Rev. E* **68**, 056304 (2003).